

The Red Sequence is Emerging at a Faster Rate Around Ultra-Red Galaxies than in the Field

A. J. R. Lewis, R. J. Ivison^{1,2}, P. N. Best¹, M. Bremer[?], J. E. Geach[?],
I. Oteo[?], J. M. Simpson[?] and A. Weiss[?]

¹*Institute for Astronomy, University of Edinburgh, Royal Observatory, Blackford Hill, Edinburgh EH9 3HJ, UK*

²*European Southern Observatory, Karl Schwarzschild Straße 2, D-85748 Garching, Germany*

Accepted XXX. Received YYY; in original form ZZZ

ABSTRACT

We selected a sample of 64 ultra-red galaxies from the S2CLS and S2COSMOS imaging surveys based on their *Herschel* photometry at their SCUBA-2 positions. Uniformly deep and wide 850- μ m data around their environments suggests that just over half of these ultra-red galaxies reside in over-dense regions of DSFGs – predominately residing near the centres ($<$ a few megaparsec) of over-densities. Weighting each surrounding DSFG by its association probability to its central ultra-red galaxy, we found that the average total dust mass was $\sim 2 \times 10^9 M_{\odot}$ – consistent with the values reported in the literature and the concept that they will evolve from high redshift ($z > 3-4$) into present-day ETGs in the cores of rich galaxy clusters. Using optical/NIR ground-based data (down to $5\text{-}\sigma_K$ depths of $\lesssim 24 \text{ mag}_{\text{AB}}$) for 42 ultra-red galaxies we were able to associate an average of ≈ 28 LBGs to within $\lesssim 5'$ of a given ultra-red galaxy. These associated LBGs showed a factor of $\approx 5\times$ and $3\times$ increase in stellar mass and absolute ($M_B - M_I$) colour respectively as their distance to the ultra-red galaxies decreased over $\approx 500 \text{ kpc}$ (or $\approx 2'$) scales – suggesting that the red sequence is beginning to emerge around ultra-red galaxies at $z \sim 3$ at a faster rate compared to the field. With an average total stellar mass contribution to the ultra-red galaxy environments from the LBGs of $4.7 \times 10^{11} M_{\odot}$, and assuming that the ultra-red galaxies convert all of their molecular gas into stars, these candidate, high-redshift proto-clusters have the potential to form systems with stellar masses of at least $M_{\text{stars}} \sim 10^{12} M_{\odot}$ by $z \sim 0$.

Key words: galaxies: clusters: general – galaxies: high-redshift – galaxies: starburst – infrared: galaxies – submillimeter: galaxies

1 INTRODUCTION

The advent of sophisticated, multiplexed, bolometer arrays sensitive to sub-millimetre (sub-mm) emission (Kreysa et al. 1998; Holland et al. 1999) facilitated the discovery of so-called ‘dusty star-forming galaxies’ (DSFGs) over two decades ago (Smail et al. 1997; Barger et al. 1998; Hughes et al. 1998; Eales et al. 1999). Obscured by vast quantities of dust (carbonaceous and amorphous silicate grains), which efficiently re-processes the ultra-violet (UV) starlight from these galaxies into far-infrared (far-IR) thermal radiation, a given DSFG is capable of producing a $M_{\text{stars}} \gtrsim 10^{11} M_{\odot}$ galaxy after an intense, merger-induced burst of star formation lasting for $t_{\text{burst}} \sim 100 \text{ Myr}$ (Lapi et al. 2014; Aversa et al. 2015). Hence, these galaxies have transformed our understanding of cosmic star formation rates (SFRs, or ψ), which until their discovery had been based predominantly on detections of UV and opti-

cally selected ‘Lyman-break galaxies’ (Steidel et al. 1996; Giavalisco 2002).

Due to their rarity, however, generating large samples of DSFGs – especially at the high-redshift ($z > 4$) tail of this population – requires expensive and time-consuming sub-mm imaging of large regions of the sky. The arrival of the *Herschel* Space Observatory (Pilbratt et al. 2010) alleviated this problem by allowing astronomers to simultaneously image large regions of the Universe at 250-, 350- and 500- μ m wavelengths with its Spectral and Photometric Imaging Receiver (SPIRE — Griffin et al. 2010) instrument. These FIR observations provided a quick and relatively inexpensive means with which to generate a large sample of distant and/or colder DSFGs based on the location of the

dust peak within their observed spectral energy distributions (SEDs¹).

In [Iverson et al. \(2016, hereafter Paper I\)](#), we followed-up a large sample of distant DSFGs – or so-called ‘ultra-red galaxies’ – with SCUBA-2 ([Holland et al. 2013](#)) from the largest ($\approx 600 \text{ deg}^2$) imaging survey undertaken with *Herschel*, *H-ATLAS* (*Herschel*-Astrophysical Terahertz Large Area Survey — [Eales et al. 2010](#)). Our ultra-red galaxies were selected based on the following criteria:

$$\overbrace{(S_{500}/S_{250} \geq 1.5) \wedge (S_{500}/S_{350} \geq 0.85)}^{\text{ultra-red}} \wedge \underbrace{(S_{500} \geq 3.5\sigma_{500})}_{\text{robust}} \wedge \underbrace{(S_{500} < 100 \text{ mJy})}_{\text{unlensed}}, \quad (1)$$

where ‘ \wedge ’ is the logical ‘and’ symbol. Hence, equation (1) clearly selects very distant – ergo ultra-red ([Cox et al. 2011](#)) – robust and largely unlensed ([Negrello et al. 2010](#)) DSFGs.

In [Paper I](#), we showed that ultra-red galaxies have a median redshift of $z \approx 3.7$ and a $z > 4$ space density of $\rho \approx 6 \times 10^{-7} \text{ Mpc}^{-3}$ – the latter being consistent with their evolution into the most massive ($M_{\text{stars}} > 10^{11} M_{\odot}$) NIR-selected galaxies at $z \sim 3.5$ ([Straatman et al. 2014](#)).

Thus, being the likely progenitors to such massive galaxies suggests that ultra-red galaxies could play an important role in the evolution and formation of large structure, i.e. galaxy clusters, within the Universe. The cores of such structures are rich with early-type galaxies (ETGs, i.e. relatively passive ellipticals and lenticulars) and mark the densest regions in the distribution of dark matter (DM). These ETGs have commonly been viewed as transformed late-type galaxies (LTGs), which have had their star formation quenched via some environmental mechanism, leaving behind an ETG on the ‘red sequence’ – an empirical relation showing that brighter, ergo more massive, galaxies are typically redder with older stellar populations and less on-going star formation ([Dressler et al. 1997](#); [Bower et al. 1998](#); [Baldry et al. 2004](#); [Gerke et al. 2007](#)).

Over-Dense regions are thought to have grown hierarchically since the decoupling of photons and matter, with initial peak positions supposedly etched into the Universe at some arbitrarily early epoch ([Peebles & Yu 1970](#); [Spergel et al. 2003](#)). In the local Universe, galaxy clusters harbour the majority of ETGs, which in turn harbour over half of the present-day stellar mass. Thus studying their cosmic evolution can place valuable constraints on models of galaxy formation ([Springel et al. 2005](#); [Robertson et al. 2007](#); [Overzier et al. 2009](#)).

Therefore, in [Lewis et al. \(2018, hereafter Paper II\)](#) we studied the 5-arcmin, far-IR environments around a representative sub-sample of ultra-red galaxies at $z \gtrsim 3$ to see if they are consistent with those expected for distant ‘proto-clusters’ – early over-densities that represent the precursors to modern-day galaxy clusters.

In [Paper II](#) we showed that the FIR environments around ultra-red galaxies are rich with bright ($S_{870} > 8 \text{ mJy}$) DSFGs compared to the field. This suggested that ultra-red galaxies could signpost candidate proto-clusters at high redshift.

Thus, these results provide a relatively straight-forward

approach to expanding the currently short list of known proto-clusters, i.e. by searching around the environments of ultra-red galaxies.

This motivates us in this paper to increase the number of potential proto-clusters by searching for ultra-red galaxies in the S2CLS and S2COSMOS imaging surveys. The 850- μm data for these two surveys are deeper and wider than those examined in [Paper II](#), which will allow us to improve upon the far-IR results reported previously. Furthermore, complementary ground-based optical/near-IR catalogues will allow us to go one step further than in [Paper II](#) and isolate any optical/near-IR galaxies around the ultra-red galaxies that are associated to them. We will examine whether these surrounding galaxies show traits consistent with residing in an over-dense environment at $z \gtrsim 3$ –4. Such traits include being able to determine whether the formation of the red sequence is happening at a faster rate around ultra-red galaxies than in the field, or whether there is any dependence on stellar mass with proximity to an ultra-red galaxy. If optical/near-IR galaxies do not show such traits it may suggest that there is something incorrect with our understanding in the formation and evolution of massive galaxies as traced by distant DSFGs.

The structure of this paper is as follows. In sections 2 and 3 we outline our ultra-red galaxy sample, as well as the far-IR analysis and results of this sample. We present our optical/near-IR analysis, results and discussion in section 4, whilst summarising and presenting our conclusions in section 5. Throughout our analysis and discussion, we adopt a ‘concordance cosmology’ with $H_0 = 71 \text{ km s}^{-1} \text{ Mpc}^{-1}$, $\Omega_m = 0.27$ and $\Omega_{\Lambda} = 0.73$ ([Hinshaw et al. 2009](#)), in which 1’ corresponds to a (proper) distance of $\approx 0.5 \text{ Mpc}$ at $z = 3$. For a quantity, x , we denote its mean and median values as x and $x_{1/2}$, respectively.

2 FIR ANALYSIS

2.1 FIR Data Acquisition and Manipulation

We used the publicly available catalogues for the S2CLS² ([Geach et al. 2017](#)) and the SCUBA-2 Cosmic Evolution Survey (S2COSMOS — [Simpson et al., in prep.](#)) imaging surveys to search for ultra-red galaxies.

The former is comprised of seven extragalactic fields: the Akari-Northern Ecliptic Pole (Akari-NEP — [Takagi et al. 2009](#)), the Cosmological Evolution Survey (COSMOS — [Scoville et al. 2007](#), which was further imaged during S2COSMOS), the Extended Groth Strip (EGS — [Groth et al. 1994](#)), the Great Observatory Origins Deep Survey-North (GOODS-N — [Wang et al. 2004](#)), the Lockman Hole North (LHN — [Dickey & Lockman 1990](#)), the Small Selected Area 22 (SSA 22 — [Lilly et al. 1991](#)) and the United Kingdom Infra-Red Telescope (UKIRT — [Casali et al. 2007](#)) Infra-Red Deep Sky Survey-Ultra Deep Survey (UKIDSS-UDS, or simply UDS — [Lawrence et al. 2007](#)). The FIR analysis that we performed required complementary *Herschel* data and we therefore discarded the

¹ Since $\lambda_{\text{obs}} = (1+z)\lambda_{\text{rest}} \sim (1+z) \times 100 \mu\text{m}$

² <https://zenodo.org/record/57792#.W0tnkRiZNE5>.

Akari-NEP and SSA 22 fields as, to the best to our knowledge, the data for these fields are either too shallow or non-existent. Thus, the five extragalactic fields analysed here cover a surveyed area of $\mathcal{A} \approx 3.7 \text{ deg}^2$ down to an instrumental r.m.s. of $\sigma_{\text{inst}} < 1.6 \text{ mJy}$. This is a factor of $\sim 4\times$ and $\sim 2\times$ improvement on the area and sensitivity considered in Paper II, respectively. The S2CLS and S2COSMOS catalogues contain 1,207 and 1,603 sources above an $850\text{-}\mu\text{m}$ SNR of $S/N > 3.5$ and $S/N > 4.0$, respectively.

2.2 PACS and SPIRE Photometry

FIR flux densities were measured on the *Herschel* PACS (100 and $160\text{ }\mu\text{m}$) and SPIRE (250, 350 and $500\text{ }\mu\text{m}$) images with PSF FWHM of $\theta = 7$ and $11.6''$ (Ibar et al. 2010) and 18, 24.8 and $35.1''$ (Nguyen et al. 2010), respectively. These images were accessed through the PACS Evolutionary Probe website³ (Lutz et al. 2011) and the *Herschel* Database in Marseille, respectively.

We extracted $2' \times 2'$ *Herschel* sub-images at the SCUBA-2 positions (which were catalogued in decreasing order of $850\text{-}\mu\text{m}$ SNR) and subsequently performed a six-dimensional Gaussian fit using the IDL MPFIT package (Markwardt 2009). During the fitting, we kept the *Herschel* FWHM fixed but allowed the Gaussian centroid (α, δ) to vary according to the $1\text{-}\sigma$ SCUBA-2 radial offset for a given SCUBA-2 source with a SNR given by:

$$\mathcal{R}_\alpha = \mathcal{R}_\delta = \frac{\mathcal{R}}{\sqrt{2}} \approx 11.2''(S/N)^{-1.6}, \quad (2)$$

where \mathcal{R} has been parameterised using equation (6) in Geach et al. (2017) to yield a similar expression to that derived in equation (B22) of Ivison et al. (2007). For each fit, we recorded the Gaussian peak flux density and corresponding $1\text{-}\sigma$ fitting error (both in units of mJy beam^{-1}). To these fitting errors, we added in quadrature the σ -clipped standard deviation of the extracted $2' \times 2'$ sub-image for the PACS measurements and confusion noises⁴ for the SPIRE measurements.

The resulting two-dimensional fits were then subtracted from their respective *Herschel* images – effectively deblending the *Herschel* images using a SCUBA-2 prior. Finally, we made no attempt to fit multiple gaussians to the *Herschel* images in cases where the SCUBA-2 detections are within a SCUBA-2 PSF of each other.

2.3 Ultra-Red Probability

In Paper II, we showed that not all of the central LABOCA sources were ultra-red after having their SPIRE photometry re-measured at their catalogued $870\text{-}\mu\text{m}$ position. This led to the introduction of a probability term that a DSFG is ultra-red (P_{UR}), which we used to isolate a robust sub-sample of ultra-red galaxies. To recap, this ‘ultra-red probability’ was derived by drawing 10,000 Gaussian realisations of the SPIRE photometry for a given DSFG and determining the fraction of these realisations that satisfied equation (1). This

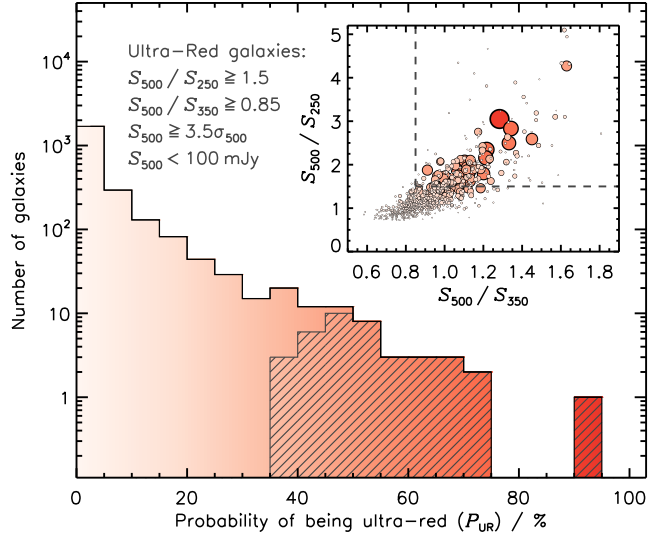


Figure 1. Main: histogram of the ultra-red probabilities for $\sim 2,000$ DSFGs in the S2CLS and S2COSMOS imaging surveys. We colour-code this histogram from light-to-dark red as the ultra-red probability increases. The ultra-red criteria clearly selects the rarest DSFGs within these two surveys – only a handful (3) have an ultra-red probability above $> 68.27\%$. The dark-grey shaded histogram represents the 39 DSFGs with SPIRE flux densities that directly satisfy equation (1). This motivated us to define an ‘ultra-red galaxy’ as a galaxy that has an ultra-red probability above $> 35\%$, which 64 galaxies satisfy. **Inset:** S_{500}/S_{250} versus S_{500}/S_{350} , colour-coded and scaled such that redder/larger circles have a higher ultra-red probability. The DSFG with the highest ultra-red probability, S2COSMOSJ100249+023255, has SPIRE flux-density ratios of $S_{500}/S_{250} \approx 3$ and $S_{500}/S_{350} \approx 1.3$ and a photometric redshift consistent with it being at $z \sim 4$. **Note.** Black dashed lines represent the ultra-red colour-cut boundaries.

method allows us to generate a robust subset of ultra-red galaxies that incorporates the photometric errors from *all* SPIRE passbands.

In Fig. 1, we show the ultra-red probability for $\sim 2,000$ DSFGs in the S2CLS and S2COSMOS imaging surveys. Motivated by the dark-grey shaded region in this figure, which represents those DSFGs whose mean SPIRE values suggest that they are ultra-red, we considered all galaxies with $P_{\text{UR}} > 35\%$ as being ultra-red. At this probability threshold, Fig. 1 indicates that there is a significant fraction (25) of DSFGs that are not directly classified as being ultra-red based on their mean SPIRE flux densities. These DSFGs are either just under the colour-cut limits and/or have larger SPIRE flux-density uncertainties.

In total, we provide a sample of 64 ultra-red galaxies, primarily from the COSMOS ($\approx 60\%$) and UDS ($\approx 30\%$) fields and the remaining from the EGS ($\approx 5\%$), GOODS-N ($\approx 2\%$) and LHN ($\approx 2\%$) fields.

In Table 1, we show how the number of ultra-red galaxies varies as we change the ultra-red probability threshold. Despite having set a fairly lenient threshold, the sample of ultra-red galaxies with $P_{\text{UR}} > 35\%$ that we present only accounts for $\approx 3\%$ of the total number of sources catalogued across both of the imaging surveys. If we were to enforce a stricter, more robust threshold of $P_{\text{UR}} \gtrsim 68\%$, we would only be left with a sample of three ultra-red galaxies – reflecting the fact that ultra-red galaxies become exponentially rarer

³ www.mpe.mpg.de/ir/Research/PEP/DR1.

⁴ The SPIRE 250-, 350- and $500\text{-}\mu\text{m}$ confusion noises are $\sigma_{\text{conf}} = 5.8, 6.3$ and 6.8 mJy , respectively (Nguyen et al. 2010).

Table 1. The number of DSFGs versus ultra-red probability threshold.

Field $N(> P_{\text{UR}} / \%)$		
	> 0	> 35	> 68.27
COSMOS	1,043	38	2
EGS	186	3	0
GOODS-N	57	1	0
LHN	189	1	0
UDS	876	21	1
	2,351	64	3

with increasing ultra-red probability. However, such a small sample of robust ultra-red galaxies prohibits any meaningful statistical analysis, which justifies the adoption of a less conservative ultra-red probability threshold in this work. Finally, it is worth mentioning that we only used the ultra-red probability to select a sample and not as a weighting for the properties analysed.

2.4 FIR Photometric Redshifts

We combined the PACS, SPIRE and SCUBA-2 flux-density measurements in order to determine FIR photometric redshifts for all $\sim 2,000$ DSFGs. We added in quadrature the confusion noise ($\sigma_{\text{conf}} = 0.8 \text{ mJy}$ — [Geach et al. 2017](#)) and calibration error ($\sigma_{\text{cal}} = 0.048 S_{\text{inst}}$, where S_{inst} is the instrumental flux density) to the de-boosted instrumental $850\text{-}\mu\text{m}$ uncertainties. The calibration uncertainty – derived from the $1\text{-}\sigma$ scatter in the peak flux conversion factors of > 500 calibrator sources ([Dempsey et al. 2013](#)) – increases the unrealistically small measurement errors for bright (likely lensed) DSFGs.

FIR photometric redshifts were derived in a similar fashion to that described in [Paper I](#) and [Paper II](#). To recap, we used three template SEDs (ALESS, the Cosmic Eyelash, and [Pope et al. \(2008\)](#)) and adopted the template that produces the lowest χ^2 over a redshift interval of $0 < z_{\text{phot}} < 10$ (down to a resolution of $\delta z_{\text{phot}} = 0.01$). In all further analysis, we used the resulting photometric redshift distribution ($P(z)$) for this best template⁵, which was derived from the best-fitting redshift values to 1,000 realisations of the FIR photometry. Adopting the entire photometric redshift distribution accounts for the (sometimes) complex shapes that they may possess better than simply adopting a Gaussian representation for them.

Finally, we draw attention to 459 DSFGs ($\approx 16\%$ of the sample) that were excluded from further analysis as their best-fitting photometric redshift values are within $\pm 1\sigma$ of a grid boundary, i.e. $\sigma^- < z_{\text{phot}} < 10 - \sigma^+$. These sources have a median $850\text{-}\mu\text{m}$ SNR and stacked de-boosted flux density of $S/N \approx 4$ and $S_{850} = 3.4 \pm 0.1$, respectively. However, they are undetected in both PACS and SPIRE, with stacked flux densities of $S_{100} = 0.0 \pm 0.1 \text{ mJy}$, $S_{160} = -0.5 \pm 0.3 \text{ mJy}$, $S_{250} = -0.5 \pm 0.2 \text{ mJy}$, $S_{350} = -0.5 \pm 0.2 \text{ mJy}$ and $S_{500} = -0.7 \pm 0.2 \text{ mJy}$. Therefore, it seems plausible that

⁵ These distributions were ‘dilated’ to take into account the template-to-template scatter in the best-fitting redshift estimates for each DSFG.

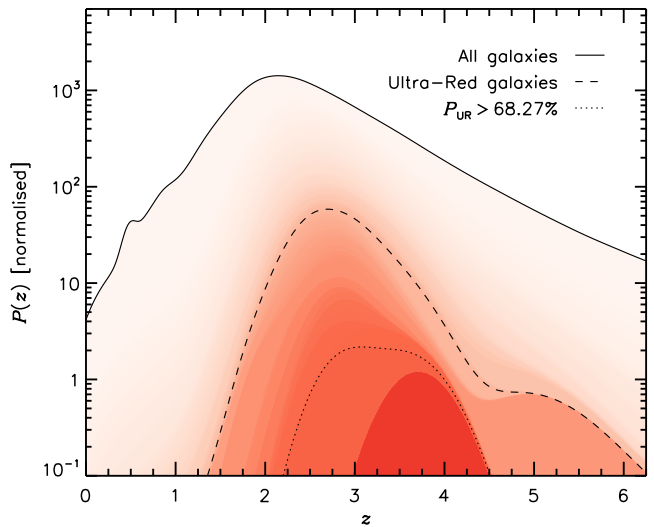


Figure 2. Sum of the photometric redshift distributions for all DSFGs (black solid line), ultra-red ($> 35\%$, black dashed line) and the robust ultra-red ($> 68.27\%$, black dotted line) galaxies. We have coloured-coded this figure such that redder colours represent the sum of the photometric redshift distributions for galaxies above a given ultra-red probability, as in Fig. 1. The general population is peaked at $z \sim 2$, whilst the ultra-red galaxy sample is shifted to $z \sim 3$. Not every DSFG above $z \gtrsim 3$ is contained within the ultra-red galaxy sample, as many of these are likely lensed ($S_{500} \geq 100 \text{ mJy}$, e.g. [Ikarashi et al. 2011](#)) or have poorly constrained SPIRE photometry. Although a very small sub-sample, the robust ultra-red galaxies are peaked closer to $z \approx 3.5$ – in strong agreement with the rigorously ‘eyeballed’ ultra-red galaxies in [Paper I](#). The reddest photometric redshift belongs to the most robust ultra-red galaxy in the sample presented here, S2COSMOSJ100249+023255.

these *Herschel* undetected sources are perhaps spurious (or very faint), which justifies the decision not to include them in any further analysis. The final sample is now based on a reduced sub-sample of $2,810 - 459 = 2,351$ DSFGs across the two imaging surveys.

In Fig. 2, we show how the sum of the photometric redshift distributions varies as the ultra-red probability is changed – highlighting where the ultra-red sub-sample and the three robust ultra-red galaxies lie. The general $850\text{-}\mu\text{m}$ -selected population peaks at $z \sim 2$, whilst the ultra-red galaxy sample presented here is shifted to $z \sim 3$ – reinforcing the effectiveness of this colour-selection technique. Interestingly, the more robust ($P_{\text{UR}} > 68.27\%$) ultra-red galaxies peak even further at $z \approx 3.5$ – in good agreement with the results presented in [Paper I](#). This reflects the smaller fraction of galaxies with (relatively) low ultra-red probabilities contained within the rigorously ‘eyeballed’, *H-ATLAS* sub-sample in [Paper I](#) than compared to here. Furthermore, this eyeballing stage, in conjunction with shallow $\sim 850\text{-}\mu\text{m}$ imaging, seems to have provided a higher fraction ($\approx 40\%$) of robust ($P_{\text{UR}} > 68.27\%$) ultra-red galaxies than presented here ($\approx 5\%$).

Finally, we derived a FIR luminosity (L_{FIR}) for each DSFG by integrating the best-fitting template SED across $8\text{--}1,000 \mu\text{m}$ in the rest frame. We converted these FIR lumi-

nosities into SFRs using

$$\frac{\psi}{M_{\odot} \text{ yr}^{-1}} \approx 1.7 \times 10^{10} \frac{L_{\text{FIR}}}{L_{\odot}}, \quad (3)$$

which assumes a Salpeter initial mass function (IMF) for star-bursting galaxies (Kennicutt 1998).

SFRs computed in this way are very sensitive to the underlying assumption made about the IMF. For instance, if a Chabrier IMF (Chabrier 2003) is assumed, which exponentially decreases the number of low mass ($\leq 1 M_{\odot}$) stars produced, then the results obtained by equation (3) would be need to be scaled down by a factor of $\approx 0.6\times$. Furthermore, there is also growing support that the IMF may actually be ‘top heavy’ within these dusty galaxies, i.e. for every high-mass star formed there would be many fewer low-mass stars formed (Baugh et al. 2005; Romano et al. 2017; Zhang et al. 2018, but see Hayward et al., 2013; Safarzadeh et al., 2017). This excess of high-mass stars also boosts the production of dust, which is necessary for increasing the FIR luminosity of these dusty galaxies. If the IMF were top heavy, then the SFRs calculated with equation (3) would be over-estimated by a factor of $\approx 3\times$.

We also computed dust masses by re-arranging the standard expression for the flux density in the optically thin (to sub-mm emission) regime (i.e. the optical depth $\tau_{\nu} \ll 1$):

$$S_{\nu}(1+z) = (1 - e^{-\tau_{\nu}}) B_{\nu}(T) \Omega_s = \tau_{\nu} B_{\nu}(T) \Omega_s, \quad (4)$$

where B_{ν} is the Planck function at a temperature T and $\Omega_s = A/D_L^2$ is the solid angle of a DSFG with a projected area A at a luminosity distance D_L . Since the optical depth is related to the opacity (κ_{ν}) and the surface area of dust mass (Σ_{dust}) as $\tau_{\nu} = \kappa_{\nu} \Sigma_{\text{dust}}$, equation (4) can be re-arranged to:

$$M_{\text{dust}} = \Sigma_{\text{dust}} A = \frac{S_{\nu}}{(1+z)\kappa_{\nu} B_{\nu}}, \quad (5)$$

where the factor of $(1+z)$ accounts for the band-shifting and compression of frequency space with redshift. We used equation (5) to determine the dust masses for all DSFGs with a photometric redshift.

3 FIR RESULTS, ANALYSIS AND DISCUSSION

We now provide an analysis on the FIR environmental properties around these 64 ultra-red galaxies within the S2CLS and S2COSMOS imaging surveys. It is worth briefly mentioning that by analysing the environments around all ultra-red galaxies, the results presented here should be free from publication bias.

3.1 Galaxy-Centric Over-Density

The first property that we considered was the galaxy-centric aperture over-density in order to examine the effectiveness of using ultra-red galaxies to signposts distant, candidate proto-clusters down to a uniform flux-density limit.

To help decide on the size of the aperture with which to measure these over-densities, we turned to the work of Chiang et al. (2013). These authors analysed the redshift-dependent properties of $\sim 3,000$ proto-clusters within the

Millennium Simulation (Springel et al. 2005), which they divided into three resulting $z = 0$ halo mass ($M_{\text{halo}}^{z=0}$) bins representing Fornax- ($M_{\text{halo}}^{z=0} = (1.37-3) \times 10^{14} M_{\odot}$), Virgo- ($M_{\text{halo}}^{z=0} = (3-10) \times 10^{14} M_{\odot}$) and Coma-type ($M_{\text{halo}}^{z=0} > 10^{15} M_{\odot}$) galaxy clusters. To quantify the spatial distribution that the smaller member halos occupied along the merger trees for a given proto-cluster at any given redshift, Chiang et al. introduced an effective radius (R_{eff}) defined as:

$$R_{\text{eff}}(z) = \sqrt{\frac{1}{M_{\text{halo}}(z)} \sum_i \Delta r_i}, \quad (6)$$

where $M_{\text{halo}}(z)$ is the total halo mass at redshift z , the sum is over all smaller member halos and Δr_i is the distance of each smaller member halo to the centre of mass of its respective proto-clusters.

Over the typical redshift range that ultra-red galaxies subtend ($2 \lesssim z \lesssim 4$), the effective radius for the most massive present-day galaxy clusters varies from $4.9' \lesssim R_{\text{eff}} \lesssim 3.8'$.

Thus, in order to be sensitive to all proto-clusters with eventual halo masses that range from $M_{\text{halo}}^{z=0} \approx 10^{14}-10^{15} M_{\odot}$, we chose an aperture with size of $R_{\text{eff}} = 4.9'$, which we represented as a peak-normalised, two-dimensional Gaussian with a FWHM of $\theta = 2R_{\text{eff}} \approx 10'$ ($\mathcal{G}_{R_{\text{eff}}}$).

The number of surrounding galaxies around each catalogued DSFG ($\mathcal{N}_{R_{\text{eff}}}$) was computed through a convolution between the aperture (centred on the position of a source) and a two-dimensional representation of these surrounding galaxies (N). In this idealised representation, each surrounding galaxies was simulated as a two-dimensional Gaussian with a centroid equal to its catalogued position and a FWHM of

$$\theta = \sqrt{8 \ln(2)} \mathcal{R},$$

i.e. each DSFG was slightly ‘smeared’ around its probable position, with the amount of smearing inversely proportional to its SNR (see equation (2)). These Gaussian representations were then normalised to their respective fidelity parameters using the catalogued FDR. As in Paper II, the signpost galaxy was removed during the measurement of $\mathcal{N}_{R_{\text{eff}}}$ in order to mitigate the bias associated with imaging a region where a galaxy is known to reside.

In order to measure the ‘expected’ number of sources around each DSFG ($\mathcal{N}'_{R_{\text{eff}}}$), we first generated a two-dimensional image for each field representing the expected number of sources at any given position. This was achieved as follows:

(i) Using the best-fitting Schechter parameters to the differential number counts suitable for a given field, we derive the number of sources expected per unit area at at a given flux density $N(S)$, allowing the flux-density to range from $S = 0.2-20.0 \text{ mJy}$.

(ii) Then, at a given value σ in the instrumental noise image of a given field, we measure how the completeness ($\mathcal{C}(S/\sigma)$) varies over this flux-density range. As this completeness was derived from simulations that used the SNR detection thresholds, it naturally accounts for the number of sources expected with low flux-density values.

(iii) The sum across all flux densities of the completeness multiplied by the number counts yields the expected number of sources per unit area, at a given value σ . Extending this to

all values in the instrumental noise image, and multiplying by the area that each value subtends (i.e. the area of a pixel, \mathcal{A}_{pix}), yields a two-dimensional representation of the number of sources expected at all positions within a given field, given by

$$N'_{\text{field}} = \sum_{\sigma} \sum_S \mathcal{C}(S/\sigma) \mathcal{A}_{\text{pix}} N(S).$$

The number of sources expected around each DSFG (N'_{eff}) is then simply the convolution of the aperture (centred on the position of that DSFG) with the applicable N'_{field} , or

$$N'_{\text{eff}} = G_{\text{eff}} * N'_{\text{field}}.$$

Finally, we scaled N'_{field} by $\sim 84\%$ in order to account for the slight deficit caused by removing $\approx 16\%$ of the sample with poorly constrained photometric redshifts. To re-iterate, generating the expected numbers of sources in this way accounts for the varying instrumental noise across a given image and thus appropriately weights regions with high-/low-instrumental noise.

In a similar method to [Paper II](#), we computed the galaxy-centric over-density parameter for each DSFG using:

$$\delta_{\text{eff}} \equiv \frac{(G_{\text{eff}} * N) - (G_{\text{eff}} * N'_{\text{field}})}{(G_{\text{eff}} * N'_{\text{field}})} = \frac{N_{\text{eff}}}{N'_{\text{eff}}} - 1, \quad (7)$$

where G_{eff} is the peak-normalised Gaussian aperture with a FWHM of $\theta = 2R_{\text{eff}}$, N is the measured spatial distribution of all DSFGs excluding the central one, and N'_{field} is the expected spatial distribution of galaxies, accounting for the varying instrumental noise values across a given field.

In [Fig. 3](#), we show a histogram and kernel density estimate (KDE) of the over-density parameter for ultra-red and not ultra-red galaxy samples. The KDE was computed by averaging many realisations of the over-density parameter for each DSFG and thus takes into account the uncertainties associated with each measurement.

We also show the normalised cumulative distribution functions (CDFs, or Φ) for the ultra-red (Φ_{UR}) and not ultra-red (Φ_{NUR}) galaxy samples, which we used to perform a two-sample Kolmogorov-Smirnov (K-S) test, defined as:

$$D_{\text{K-S}} = \sup_{\delta_{\text{eff}}} |\Phi_{\text{UR}}(\delta_{\text{eff}}) - \Phi_{\text{NUR}}(\delta_{\text{eff}})|, \quad (8)$$

where $D_{\text{K-S}}$ is the maximum distance between the two CDFs. This distance quantifies the probability that two CDFs are randomly drawn from the same population.

We derived a value of $D_{\text{K-S}} = 0.12$, which equates to a probability of $P_{\text{K-S}} \sim 15\%$ that ultra-red and not ultra-red galaxies are drawn from the same over-density parameter distribution. Therefore, the differences are slight ($\gtrsim 1\sigma$) between the two samples. It appears that not all ultra-red galaxies signpost over-dense regions and $\approx 40\%$ of them lie in under-dense regions ($\delta_{\text{eff}} \leq 0$) compared to $\approx 50\%$ of the galaxies that are not ultra-red. These results are somewhat similar to those found in [Paper II](#) for bright ($S > 8\text{mJy}$) DSFGs.

Finally, [Fig. 4](#), which is continued in the appendix, shows the over-density and SPIRE false-colour cut-outs for ultra-red galaxies with $P_{\text{UR}} > 60\%$. The former indicate where the ultra-red galaxies lie in relation to their closest over-density peaks.

3.2 Proximity to Closest Over-Density Peak

As discussed, $\approx 60\%$ of ultra-red galaxies reside in over-dense regions, which motivated us to examine the exact locations in these environments that they occupy. For example, are these ‘over-dense’ ultra-red galaxies situated near to the centres of ‘high-value’ over-density peaks, which would be consistent with them signposting the most extreme nodes in the DM distribution? Or, is the situation closer to them signposting less extreme over-densities forming within the filamentary structure?

To answer this question, we used *all* of the catalogued DSFGs in a given field to generate a ‘global’ over-density image, which I used to search for ‘global peaks’ that are above $\delta_{\text{eff}} > 0$. These global peaks were detected and extracted using the same source extraction algorithm described in the [Paper II](#), i.e. searching for peaks in a top-down fashion that are separated by a distance of $2R_{\text{eff}}$ from each other and the image edges. The resulting global peaks were then normalised to the maximum value of the extracted peaks. All extracted peaks were subsequently categorised as having either a low, medium or high value, corresponding to $0 < \delta_{\text{eff}}/\max(\delta_{\text{eff}}) < 1/3$, $1/3 < \delta_{\text{eff}}/\max(\delta_{\text{eff}}) < 2/3$ and $2/3 < \delta_{\text{eff}}/\max(\delta_{\text{eff}}) < 1$, respectively. We then analysed the radial distribution of ultra-red galaxies to their closest global peak, under the assumption that medium-to-high-value global over-density peaks may represent extreme nodes in the DM distribution, whilst low-value global over-density peaks represent the less extreme over-densities with the filamentary structure.

In [Fig. 5](#), we show this radial distribution for $\approx 60\%$ of the ultra-red galaxies that show a positive ($\delta_{\text{eff}} > 0$) over-density. The closest global peaks to around $\sim 2/3$ of these galaxies are of medium or high value. All ultra-red galaxies closest to a medium-value peak are distributed over $1.5R_{\text{eff}} \approx 7'$ (or $\sim 3\text{Mpc}$ at $z = 3$) scales, suggesting that they play a central role in these over-densities. The situation is different for the high-value peaks as only $\approx 65\%$ of the ultra-red galaxies are distributed within $1.5R_{\text{eff}}$ scales – with some being as far out as $4R_{\text{eff}} \approx 15'$.

In the low-value peaks, which $\sim 1/3$ of the $\approx 60\%$ of ultra-red galaxies occupy, they primarily tend to be within $0.5R_{\text{eff}}$ (or $\sim 1\text{Mpc}$ at $z = 3$) of the peak position. Thus, ultra-red galaxies are mainly situated in the centres of low-valued over-density regions. These findings may suggest that around $\approx 20\%$ of ultra-red galaxies are signposting less extreme over-densities within filamentary structures, rather than the extreme nodes.

3.3 Previously Identified Proto-Clusters

A comprehensive review of previously identified/confirmed proto-clusters is given in [Casey \(2016\)](#), but we now briefly outline those found within some of the fields that we have analysed in this chapter.

- A proto-cluster containing seven DSFGs at $z \sim 2.5$ within the COSMOS field was serendipitously unveiled by [Casey et al. \(2015\)](#). Situated in the centre and $\approx 10'$ north of this over-density are the ultra-red galaxies S2COSMOSJ100025+022605 and S2COSMOSJ100013+023429, respectively. Although not

officially catalogued as part of this proto-cluster, these ultra-red galaxies have photometric redshifts of $z_{\text{phot}} = 2.95^{+0.36}_{-0.30}$ and $z_{\text{phot}} = 2.77^{+0.33}_{-0.29}$, respectively. Thus, it is not inconceivable that these two ultra-red galaxies are members of this $z \sim 2.5$ structure (rather than residing behind it). Interestingly, none of the catalogued members of this structure meet the strict ultra-red criteria. Furthermore, the environment around S2COSMOSJ100025+022605 (at the heart this Casey et al. structure) shows no particular over-/under-density of DSFGs compared to the field over the ~ 5 -arcmin scales that we have examined.

- Hung et al. (2016) report a proto-cluster containing nine DSFGs at $z \approx 2.1$ within the COSMOS field, $\approx 10'$ south of the Casey et al. structure.

- There is another confirmed proto-cluster within the COSMOS field containing four galaxies at $z \approx 5.3$ (the AzTEC-3 over-density — Capak et al. 2011; Riechers et al. 2010). However, these galaxies are all contained within a single SCUBA-2 PSF, known as ‘COSMOS AzTEC-3’.

- Finally, there are five DSFGs comprising a proto-cluster in the GOODS-N field at $z = 1.99$ (Blain et al. 2004; Chapman et al. 2009).

These previously identified proto-clusters provide a sample of 16 spectroscopically confirmed DSFGs within $z \sim 2$ – 2.5 , which we used to measure the accuracy of the photometric redshift technique using the familiar expression

$$\Delta z / (1 + z_{\text{spec}}) \equiv (z_{\text{phot}} - z_{\text{spec}}) / (1 + z_{\text{spec}}).$$

We found an accuracy and dispersion of $\mu_{|\Delta z|} \sim 0.1 \times (1 + z_{\text{spec}})$ and $\sigma_{\Delta z} \sim 0.1 \times (1 + z_{\text{spec}})$, respectively, re-iterating the predictive power of our photometric redshift algorithm, especially in this redshift interval. These results are broadly consistent with those found in Paper I and Paper II.

Although this is only a small spectroscopic sample, these results are slightly more accurate, and reliable, than those achieved by Michałowski et al. (2017) for these same DSFGs, namely $\mu_{|\Delta z|} \sim 0.2 \times (1 + z_{\text{spec}})$ and $\sigma_{\Delta z} \sim 0.3 \times (1 + z_{\text{spec}})$, respectively.

3.4 Associations Based on Photometric Redshifts

The observed redshift ($1 + z_{\text{obs}}$) of a given galaxy (typically determined by frequency shifts in its observed spectrum, $\nu_{\text{rest}}/\nu_{\text{obs}}$) is composed of a (dominant) cosmological factor due to the expansion of space ($1 + z_{\text{cos}}$), a peculiar factor due to the velocity of that galaxy with respect to an observer (i.e. the Doppler effect, $1 + z_{\text{pec}}$) and a gravitational factor due to the influence of strong gravitational fields in its vicinity ($1 + z_{\text{grav}}$) as follows:

$$\frac{\nu_{\text{rest}}}{\nu_{\text{obs}}} = (1 + z_{\text{obs}}) = (1 + z_{\text{cos}})(1 + z_{\text{pec}})(1 + z_{\text{grav}}). \quad (9)$$

Thus, testing whether a particular DSFG at a redshift z is ‘associated’ to another galaxy relies on being able to constrain their observed redshifts to within:

$$|\Delta z|_{\text{assoc}} \lesssim \frac{2\sigma_{\text{los}}}{c}(1 + z), \quad (10)$$

where σ_{los} is line-of-sight velocity dispersion. The typical velocity dispersion for (unvirialised) members of a distant ($z \gtrsim 3$) proto-cluster is around $\sigma_{\text{los}} \approx 500 \text{ km s}^{-1}$, but values as high as $\sigma_{\text{los}} \approx 2,000 \text{ km s}^{-1}$ have been recorded

(Venemans et al. 2007; Dey et al. 2016). Finally, it is important to note that equation (10) assumes that the two galaxies are at the same cosmological redshift (z) and neglects the effects from strong gravitational fields. Furthermore, the factor of 2 accounts for the fact that these two galaxies may be placed at opposing ends of a given structure when imaged.

In Paper II, we associated galaxies within the same structure using an association threshold of $|\Delta z|_{\text{assoc}} \lesssim 0.5$, which was based on the median photometric-redshift fitting errors for $z \sim 3$ DSFGs using shallow FIR photometry. However, not only is this threshold an order of magnitude greater than that expected from equation (10) using the maximum velocity dispersion recorded in proto-clusters, this method also treated two DSFGs that were ‘associated’ to a particular structure signposted by an ultra-red galaxy the same, regardless of how well their individual photometric redshifts were constrained.

Thus, we have taken a different approach in this work and used the photometric redshift probability distributions and equation (10) to assign each surrounding galaxy an ‘associated probability’ ($\mathcal{P}_{\text{assoc}}$). This probability was calculated by drawing 10,000 redshift realisations from each photometric redshift distribution and determining the number of times that equation (10) was satisfied. Furthermore, we subsequently assigned each surrounding galaxy an ‘association weight’ ($\mathcal{W}_{\text{assoc}}$), which was simply the association probability scaled by the fidelity of that particular galaxy.

For instance, the probability that one ultra-red galaxy is associated to another ultra-red galaxy (assuming that each have a photometric redshift of $z_{\text{phot}} = 2.80 \pm 0.19$ and neglecting the $\sigma_z = 0.14(1 + z) \sim 0.5$ intrinsic template SED scatter) to within $|\Delta z|_{\text{assoc}} \lesssim 0.05$ is $\mathcal{P}_{\text{assoc}} \sim 15\%$. Furthermore, assuming that this ultra-red galaxy has a fidelity parameter of $\mathcal{F} = 0.8$, we would assign this particular surrounding galaxy an association weight of $\mathcal{W}_{\text{assoc}} \sim 10\%$.

We were only able to associate (on average) ≈ 1 surrounding DSFG to an ultra-red galaxy, which was determined by summing the association weights from all of its surrounding galaxies within $R_{\text{eff}} \sim 5'$. Interestingly, this is the same average number of associations achieved in Paper II, which is perhaps indicative of the limitations with using FIR-based photometric redshifts.

3.5 FIR Total Dust Masses and SFRs

With a method for weighting the contributions from any surrounding DSFGs using equation (10), we derived the total dust masses and total SFRs within the 5-arcmin environments around the ultra-red galaxies catalogued in the S2CLS and S2COSMOS imaging surveys. We show the results of these two properties in the top and bottom panels of Fig. 6, respectively, noting that these values exclude the contributions from the central ultra-red galaxies.

The total dust masses peak at $M_{\text{dust}} \approx 1.8 \times 10^9 M_{\odot}$, whilst the total SFRs peak at $\Psi \approx 1,400 M_{\odot} \text{ yr}^{-1}$. These values are broadly consistent with those reported in Paper II, namely $M_{\text{dust}} \sim 1.7 \times 10^9 M_{\odot}$ and $\Psi \approx 1,100 M_{\odot} \text{ yr}^{-1}$, respectively, somewhat expected due to the same number of associated DSFGs.

As the expected number of galaxies within an aperture around any given DSFG varies – reflective of the differing image r.m.s. values and/or edge effects – we also computed

the ‘missing’ number of galaxies necessary to reconcile the shallowest regions with the deepest regions in an image. We represented these missing DSFGs with the global photometric redshift distribution (see Fig. 2), average dust masses of $1.2 \times 10^9 M_\odot$ and average SFRs of $575 M_\odot \text{ yr}^{-1}$, with the latter two being computed using the method outlined in Barlow (2004). However, the effect of including these missing galaxies was small, namely it increased the total dust masses and total SFRs by a factor of $\sim 1.25\times$ to $M_{\text{dust}} \approx 2.2 \times 10^9 M_\odot$ and $\Psi \approx 1,600 M_\odot \text{ yr}^{-1}$, respectively.

Finally, it is worth mentioning that total dust masses and total SFRs computed via this method converged as the association weight of surrounding galaxies tended to zero ($\mathcal{W}_{\text{assoc}} \rightarrow 0$), suggesting that including all of the surrounding galaxies in this calculation was reasonable.

4 OPTICAL/NIR ANALYSIS

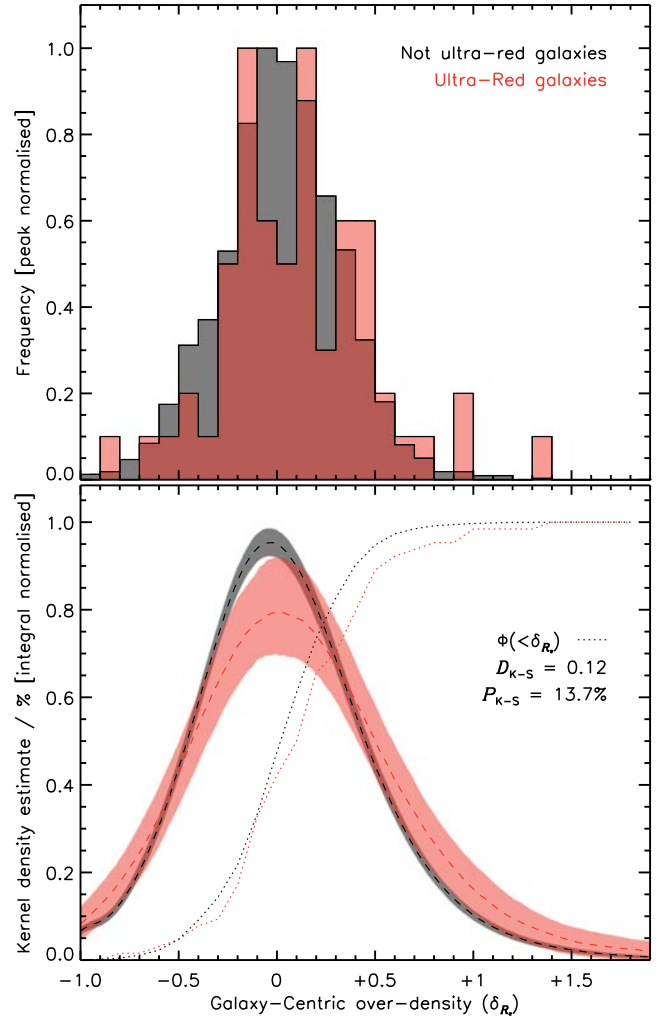


Figure 3. **Top:** peak-normalised histograms of the over-density parameter for ultra-red (red) and not ultra-red (black) galaxies. Each over-density parameter is calculated within an effective radius of $R_{\text{eff}} \approx 5'$ centred on each galaxy. We ensured that the central galaxy is removed from this calculation in order to reduce the galaxy-centric bias. The distribution for ultra-red galaxies appears to be slightly shifted towards higher over-density parameter values. **Bottom:** KDE of the over-density parameter for both samples derived by averaging 1,000 realisations of the over-density parameter for each DSFG. The shaded regions represent the r.m.s. scatter across these realisations. A slight ($\gtrsim 1\sigma$) excess is present in regions with higher ($\delta_{R_{\text{eff}}} \gtrsim 1$) over-density parameter values. Clearly not all ultra-red galaxies signpost over-dense regions, but there exists a growing separation between the two samples that becomes more pronounced around $\delta_{R_{\text{eff}}} \approx 0.5\text{--}1.5$. This indicates that ultra-red galaxies preferentially signpost regions with greater over-density parameter values than galaxies that are not ultra-red, as found in the Paper II. We over-plot the normalised CDFs (dashed lines) for these two samples, which highlights this divergence more clearly. A K-S test using the CDFs indicates that there is a $\approx 15\%$ chance that the two distributions are the same.

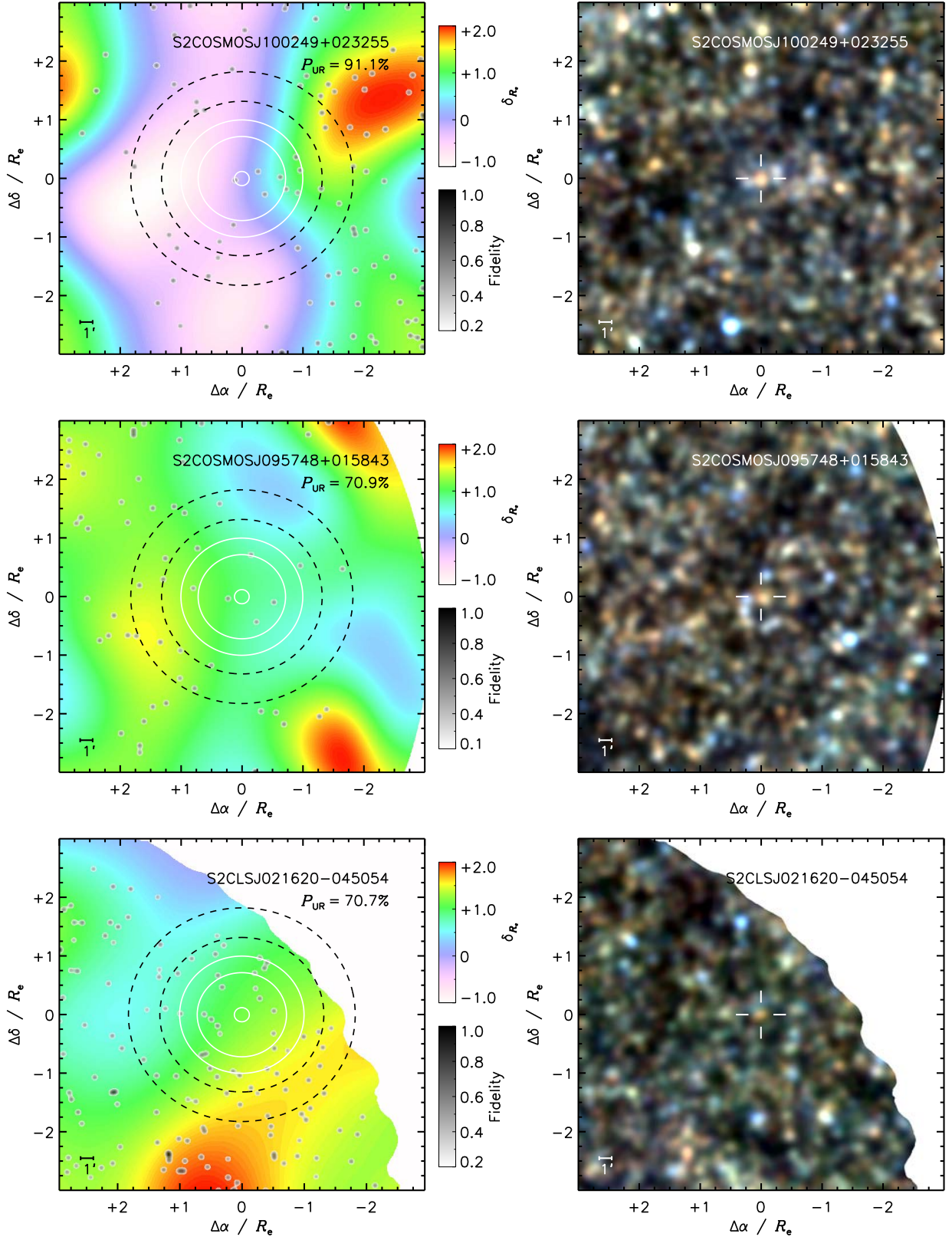


Figure 4. Left: $6R_{\text{eff}} \times 6R_{\text{eff}}$ cut-outs ($R_{\text{eff}} \approx 5'$) of the over-density parameter for galaxies with an ultra-red probability above $P_{UR} > 60\%$. These cut-outs are colour-coded such that bluer/redder regions represent lower/higher over-density values. Surrounding DSFGs are shown in black as Gaussian PSFs with FWHM of $\theta = 14''$ that are integral normalised to their respective fidelity parameters. I show contours representing the 10, 30 (dashed black), 50, 70 and 99% (white) values of the Gaussian aperture adopted, i.e. the aperture FWHM of $\theta = 2R_{\text{eff}}$ is indicated by the furthestmost white contour. Right: SPIRE false-colour cut-outs of the same regions. The 250- and 350- μm images have been filtered to the 500- μm resolution. A white cursor indicates the central ultra-red galaxy within each cut-out. **Note.** — Ultra-Red galaxies are presented in order of decreasing ultra-red probability. A distance scale is shown in the bottom left corner of each cut-out. This figure is continued in appendix A for the six extra ultra-red galaxies with $P_{UR} > 60\%$.

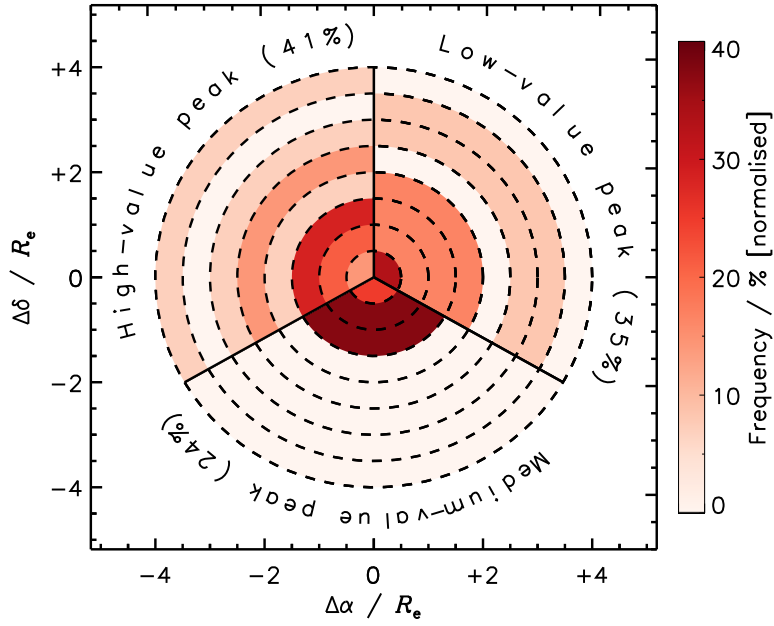


Figure 5. Radial distance of the $\sim 60\%$ of ultra-red galaxies that show a positive over-density parameter to their closest global over-density peak. These peaks are divided into low, medium and high values (solid black lines) that are represented by three segments with radial offsets that increment by $0.5R_{\text{eff}} \approx 2'$ (dashed black lines). The majority ($\approx 60\%$) of over-dense ultra-red galaxies are located next to a medium- or high-value peak. Those nearest to a medium-value peak are all distributed within $< 1.5R_{\text{eff}} \approx 7'$ (or 3 Mpc at $z \sim 3$) of the peak position – suggesting that these ultra-red galaxies may play a dominant role in such environments. On the other hand, only $\sim 2/3$ of ultra-red galaxies that are nearest to a high-value peak are distributed within a similar scale and the remaining $\sim 1/3$ are distributed as far out as $\approx 4R_{\text{eff}} \approx 20'$. A similar picture is seen for the $\approx 33\%$ of over-dense ultra-red galaxies that are closest to a low-value peak, although a slight enhancement is seen within the inner-most radial bin.

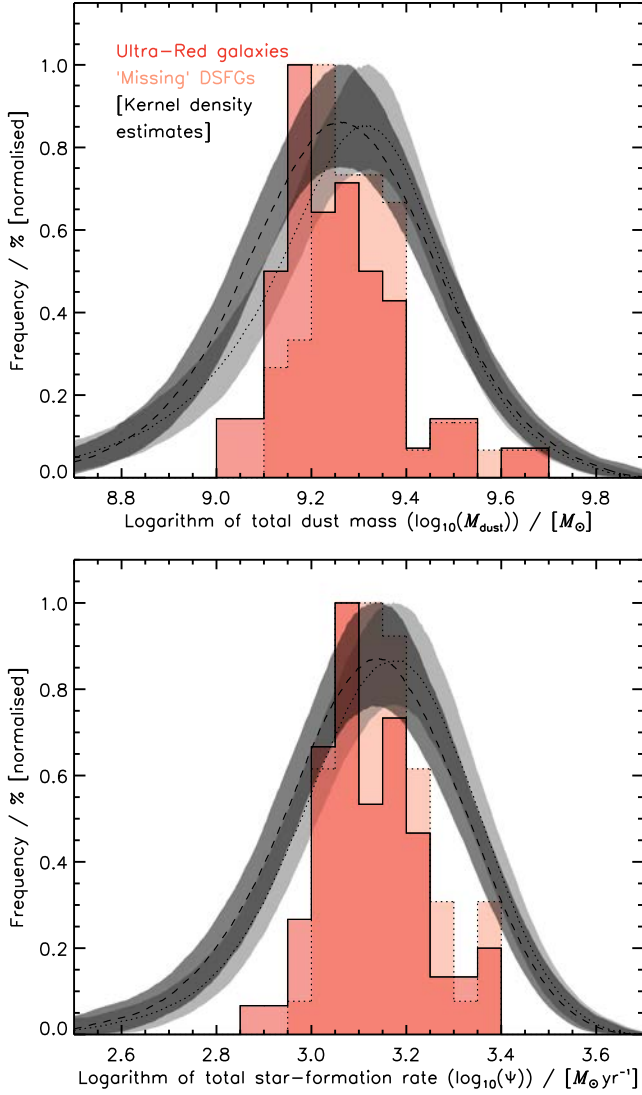


Figure 6. Top: histogram of the total dust masses around ultra-red galaxies (red) and an arbitrarily normalised KDE (black), which was derived by averaging 1,000 realisations of the total dust masses for the surrounding galaxies. Each surrounding DSFG within $R_{\text{eff}} \approx 5'$ has been weighted according to equation (10). The total dust mass peaks at $\approx 2 \times 10^9 M_{\odot}$ – equating to a molecular-gas reservoir of $\sim 10^{11} M_{\odot}$, assuming a GDR of $\delta_{\text{GDR}} = 100$. The dotted black lines show the effect of accounting for the ‘missing’ DSFGs due to varying r.m.s. values around each ultra-red galaxy. These missing DSFGs increase the total dust mass in the environments of ultra-red galaxies by a factor of $\sim 1.25\times$. **Bottom:** histogram (red) and normalised KDE (black) of the total SFR for DSFGs in the $R_{\text{eff}} \approx 5$ -arcmin vicinity of ultra-red galaxies. Again, each SFR has been weighted accordingly and a contribution from the missing DSFGs has also been shown (dark grey). The peak of this distribution occurs at a total SFR of $\Psi \sim 1,100 M_{\odot} \text{yr}^{-1}$, which – assuming a 100-Myr burst of star formation – could easily result in a present-day structure with total stellar mass of $M_{\text{stars}} \sim 10^{11} M_{\odot}$.

Table 2. Ultra-Red galaxies and their environmental properties.

IAU	Field	z	P_{UR} %	$\Sigma \mathcal{F}$	$\delta_{\text{R eff}}^{\dagger}$	$\Sigma \mathcal{P}_{\text{assoc}}^{\dagger}$	$\log_{10}(M_{\text{dust}})^{\dagger}$ [M_{\odot}]	$\log_{10}(\Psi)^{\dagger}$ [$M_{\odot} \text{ yr}^{-1}$]	$\Sigma \mathcal{P}_{\text{assoc}}$	$\delta_{\text{R eff}}$	$\log_{10}(M_{\text{stars}})$ [M_{\odot}]
FIR						Optical/NIR					
S2COSMOSJ100249+023255	COSMOS	$3.72^{+0.35}_{-0.33}$	$91.1^{+0.3}_{-0.3}$	$8.7^{+4.0}_{-2.8}$	$+0.3^{+0.6}_{-0.4}$	$0.2^{+0.1}_{-0.1}$	$9.5^{+0.1}_{-0.1}$	$3.4^{+0.1}_{-0.1}$	$10.5^{+1.0}_{-1.3}$	$-0.1^{+0.3}_{-0.2}$	11.2
S2COSMOSJ095748+015843	COSMOS	$3.25^{+0.40}_{-0.34}$	$70.9^{+0.3}_{-0.3}$	$4.8^{+3.3}_{-2.1}$	$-0.2^{+0.6}_{-0.4}$	$0.3^{+0.2}_{-0.1}$	$9.3^{+0.1}_{-0.1}$	$3.1^{+0.1}_{-0.1}$	$22.3^{+2.2}_{-2.6}$	$+0.1^{+0.3}_{-0.2}$	11.5
S2CLSJ021620-045054	UDS	$2.85^{+0.32}_{-0.28}$	$70.7^{+0.3}_{-0.3}$	$16.7^{+4.9}_{-3.9}$	$-0.4^{+0.2}_{-0.1}$	$0.6^{+0.2}_{-0.2}$	$9.2^{+0.2}_{-0.2}$	$3.1^{+0.2}_{-0.2}$	$15.3^{+2.7}_{-1.4}$	$-0.1^{+0.1}_{-0.1}$	11.5
S2COSMOSJ100209+023633	COSMOS	$3.22^{+0.36}_{-0.32}$	$68.1^{+0.3}_{-0.3}$	$13.5^{+4.7}_{-3.6}$	$+0.9^{+0.7}_{-0.5}$	$0.4^{+0.1}_{-0.1}$	$9.3^{+0.1}_{-0.1}$	$3.2^{+0.1}_{-0.1}$	$29.0^{+2.0}_{-3.6}$	$+0.3^{+0.5}_{-0.3}$	11.6
S2COSMOSJ100323+023352	COSMOS	$2.73^{+0.27}_{-0.26}$	$67.9^{+0.3}_{-0.3}$	$1.0^{+2.3}_{-0.8}$	$-0.8^{+0.4}_{-0.1}$	$0.3^{+0.8}_{-0.3}$	$9.3^{+0.1}_{-0.1}$	$3.2^{+0.1}_{-0.1}$	—	—	—
S2COSMOSJ100235+024731	COSMOS	$2.88^{+0.35}_{-0.29}$	$65.4^{+0.3}_{-0.3}$	$9.9^{+4.2}_{-3.1}$	$+0.6^{+0.7}_{-0.5}$	$0.6^{+0.2}_{-0.2}$	$9.2^{+0.2}_{-0.2}$	$3.1^{+0.2}_{-0.2}$	$34.1^{+3.1}_{-3.9}$	$+0.2^{+0.4}_{-0.3}$	11.7
S2COSMOSJ095931+023043	COSMOS	$2.87^{+0.28}_{-0.26}$	$64.6^{+0.3}_{-0.3}$	$9.6^{+4.1}_{-3.0}$	$+0.1^{+0.5}_{-0.3}$	$0.4^{+0.1}_{-0.1}$	$9.3^{+0.1}_{-0.1}$	$3.1^{+0.1}_{-0.1}$	$28.6^{+2.4}_{-3.9}$	$+0.2^{+0.5}_{-0.3}$	11.6
S2CLSJ021631-052622	UDS	$2.79^{+0.27}_{-0.25}$	$61.8^{+0.2}_{-0.2}$	$16.5^{+5.1}_{-4.0}$	$-0.1^{+0.3}_{-0.2}$	$0.6^{+0.1}_{-0.1}$	$9.3^{+0.1}_{-0.1}$	$3.2^{+0.1}_{-0.1}$	—	—	—
S2COSMOSJ100257+014257	COSMOS	$2.58^{+0.30}_{-0.27}$	$60.2^{+0.2}_{-0.2}$	$5.0^{+3.4}_{-2.1}$	$-0.1^{+0.6}_{-0.4}$	$0.6^{+0.4}_{-0.2}$	$9.2^{+0.1}_{-0.2}$	$3.1^{+0.1}_{-0.2}$	—	—	—
S2COSMOSJ100115+024257	COSMOS	$2.44^{+0.23}_{-0.23}$	$56.5^{+0.2}_{-0.2}$	$6.9^{+3.7}_{-2.5}$	$-0.2^{+0.4}_{-0.3}$	$0.6^{+0.3}_{-0.2}$	$9.3^{+0.1}_{-0.1}$	$3.2^{+0.1}_{-0.1}$	$52.8^{+3.6}_{-4.3}$	$+0.2^{+0.4}_{-0.3}$	12.0
S2COSMOSJ095738+015813	COSMOS	$3.02^{+0.35}_{-0.32}$	$56.4^{+0.2}_{-0.2}$	$4.9^{+3.3}_{-2.1}$	$+1.4^{+1.6}_{-1.0}$	$0.5^{+0.3}_{-0.2}$	$9.3^{+0.1}_{-0.1}$	$3.1^{+0.1}_{-0.1}$	$19.8^{+2.6}_{-3.5}$	$-0.2^{+0.3}_{-0.2}$	11.5
S2COSMOSJ100140+023011	COSMOS	$2.76^{+0.44}_{-0.38}$	$55.2^{+0.2}_{-0.2}$	$4.9^{+3.3}_{-2.1}$	$-0.4^{+0.4}_{-0.3}$	$0.4^{+0.2}_{-0.2}$	$9.2^{+0.2}_{-0.2}$	$3.0^{+0.2}_{-0.2}$	$46.9^{+2.5}_{-4.3}$	$+0.3^{+0.5}_{-0.3}$	11.9
S2COSMOSJ100142+014033	COSMOS	$2.87^{+0.30}_{-0.27}$	$52.5^{+0.2}_{-0.2}$	$6.9^{+3.7}_{-2.5}$	$+0.1^{+0.4}_{-0.4}$	$0.6^{+0.3}_{-0.2}$	$9.4^{+0.1}_{-0.1}$	$3.2^{+0.1}_{-0.1}$	$26.4^{+2.6}_{-4.8}$	$-0.2^{+0.4}_{-0.2}$	11.6
S2CLSJ141715+523630	EGS	$2.70^{+0.30}_{-0.27}$	$51.5^{+0.2}_{-0.2}$	$10.5^{+4.2}_{-3.1}$	$+0.3^{+0.5}_{-0.4}$	$0.6^{+0.3}_{-0.2}$	$9.3^{+0.1}_{-0.2}$	$3.1^{+0.1}_{-0.2}$	—	—	—
S2CLSJ021730-045936	UDS	$2.82^{+0.25}_{-0.24}$	$51.4^{+0.2}_{-0.2}$	$18.9^{+5.3}_{-4.2}$	$-0.0^{+0.3}_{-0.2}$	$0.5^{+0.1}_{-0.1}$	$9.3^{+0.1}_{-0.1}$	$3.2^{+0.1}_{-0.1}$	$21.8^{+2.0}_{-2.4}$	$-0.1^{+0.1}_{-0.1}$	11.5
S2CLSJ104456+584959	LHN	$2.82^{+0.31}_{-0.29}$	$51.3^{+0.2}_{-0.2}$	$9.0^{+3.8}_{-2.8}$	$-0.2^{+0.4}_{-0.3}$	$0.3^{+0.1}_{-0.1}$	$9.4^{+0.1}_{-0.1}$	$3.1^{+0.1}_{-0.1}$	—	—	—
S2CLSJ021940-045618	UDS	$2.09^{+0.21}_{-0.23}$	$51.0^{+0.2}_{-0.2}$	$20.2^{+5.4}_{-4.4}$	$+0.2^{+0.3}_{-0.3}$	$1.0^{+0.3}_{-0.2}$	$9.2^{+0.1}_{-0.2}$	$3.1^{+0.1}_{-0.2}$	—	—	—
S2COSMOSJ100207+024137	COSMOS	$2.55^{+0.30}_{-0.28}$	$50.6^{+0.2}_{-0.2}$	$10.6^{+4.3}_{-3.2}$	$+0.6^{+0.7}_{-0.5}$	$0.7^{+0.3}_{-0.2}$	$9.3^{+0.1}_{-0.2}$	$3.1^{+0.1}_{-0.2}$	$45.5^{+4.3}_{-3.8}$	$+0.2^{+0.5}_{-0.3}$	11.9
S2CLSJ021744-052008	UDS	$3.20^{+0.36}_{-0.28}$	$50.4^{+0.2}_{-0.2}$	$20.8^{+5.5}_{-4.4}$	$+0.0^{+0.3}_{-0.2}$	$0.6^{+0.2}_{-0.1}$	$9.4^{+0.2}_{-0.2}$	$3.2^{+0.2}_{-0.1}$	$12.6^{+1.1}_{-1.4}$	$-0.0^{+0.1}_{-0.1}$	11.3
S2COSMOSJ095821+015937	COSMOS	$3.01^{+0.38}_{-0.30}$	$50.2^{+0.2}_{-0.2}$	$7.7^{+3.8}_{-2.7}$	$+0.1^{+0.5}_{-0.4}$	$0.5^{+0.2}_{-0.2}$	$9.2^{+0.2}_{-0.2}$	$3.1^{+0.2}_{-0.2}$	$33.7^{+2.6}_{-3.9}$	$+0.2^{+0.4}_{-0.2}$	11.8
S2COSMOSJ100136+021109	COSMOS	$2.79^{+0.27}_{-0.24}$	$49.0^{+0.2}_{-0.2}$	$17.5^{+5.2}_{-4.1}$	$+0.2^{+0.3}_{-0.3}$	$0.9^{+0.3}_{-0.2}$	$9.3^{+0.2}_{-0.2}$	$3.2^{+0.2}_{-0.1}$	$38.1^{+3.2}_{-4.9}$	$+0.3^{+0.5}_{-0.3}$	11.8
S2COSMOSJ100153+021941	COSMOS	$2.47^{+0.26}_{-0.25}$	$48.1^{+0.2}_{-0.2}$	$18.4^{+5.3}_{-4.2}$	$+0.5^{+0.4}_{-0.3}$	$0.9^{+0.3}_{-0.2}$	$9.2^{+0.2}_{-0.2}$	$3.1^{+0.2}_{-0.2}$	$33.0^{+2.7}_{-5.8}$	$+0.1^{+0.4}_{-0.2}$	11.8
S2COSMOSJ100059+013307	COSMOS	$4.93^{+0.76}_{-0.45}$	$48.0^{+0.2}_{-0.2}$	$4.9^{+3.3}_{-2.1}$	$+0.7^{+1.1}_{-0.8}$	$0.1^{+0.1}_{-0.0}$	$9.7^{+0.1}_{-0.1}$	$3.4^{+0.1}_{-0.1}$	—	—	—
S2COSMOSJ100317+024944	COSMOS	$2.75^{+0.26}_{-0.25}$	$47.1^{+0.2}_{-0.2}$	$3.0^{+2.9}_{-1.6}$	$+0.4^{+1.3}_{-0.8}$	$0.8^{+0.7}_{-0.4}$	$9.4^{+0.1}_{-0.1}$	$3.3^{+0.1}_{-0.1}$	—	—	—
S2COSMOSJ100025+022605	COSMOS	$2.95^{+0.25}_{-0.30}$	$47.1^{+0.2}_{-0.2}$	$35.3^{+6.9}_{-5.9}$	$-0.1^{+0.2}_{-0.2}$	$1.0^{+0.2}_{-0.2}$	$9.3^{+0.2}_{-0.2}$	$3.2^{+0.2}_{-0.2}$	$27.8^{+2.3}_{-3.7}$	$+0.0^{+0.4}_{-0.2}$	11.7
S2CLSJ021556-052106	UDS	$2.46^{+0.21}_{-0.20}$	$46.6^{+0.2}_{-0.2}$	$17.4^{+5.0}_{-4.0}$	$+0.3^{+0.4}_{-0.3}$	$0.8^{+0.2}_{-0.2}$	$9.4^{+0.1}_{-0.1}$	$3.3^{+0.1}_{-0.1}$	—	—	—
S2CLSJ021702-052718	UDS	$2.22^{+0.31}_{-0.33}$	$46.3^{+0.2}_{-0.2}$	$21.0^{+5.4}_{-4.3}$	$+0.1^{+0.3}_{-0.2}$	$0.9^{+0.2}_{-0.2}$	$9.1^{+0.2}_{-0.2}$	$3.0^{+0.2}_{-0.2}$	$38.0^{+3.2}_{-3.1}$	$-0.1^{+0.1}_{-0.1}$	11.9
S2COSMOSJ095946+015715	COSMOS	$3.08^{+0.34}_{-0.29}$	$46.2^{+0.2}_{-0.2}$	$12.7^{+4.6}_{-3.5}$	$+0.3^{+0.5}_{-0.4}$	$0.6^{+0.2}_{-0.2}$	$9.3^{+0.2}_{-0.1}$	$3.2^{+0.1}_{-0.1}$	$29.5^{+2.3}_{-2.7}$	$-0.0^{+0.3}_{-0.2}$	11.6
S2CLSJ021724-044030	UDS	$2.65^{+0.31}_{-0.28}$	$46.1^{+0.2}_{-0.2}$	$13.9^{+4.6}_{-3.5}$	$-0.2^{+0.3}_{-0.2}$	$0.7^{+0.2}_{-0.2}$	$9.2^{+0.2}_{-0.2}$	$3.1^{+0.2}_{-0.2}$	$17.5^{+2.8}_{-2.3}$	$-0.1^{+0.1}_{-0.1}$	11.5
S2CLSJ123633+621408	GOODS-N	$2.97^{+0.25}_{-0.23}$	$45.6^{+0.2}_{-0.2}$	$23.6^{+5.7}_{-4.7}$	$+0.4^{+0.3}_{-0.3}$	$0.9^{+0.2}_{-0.2}$	$9.4^{+0.1}_{-0.1}$	$3.2^{+0.1}_{-0.1}$	—	—	—
S2CLSJ021753-051100	UDS	$2.61^{+0.27}_{-0.25}$	$45.2^{+0.2}_{-0.2}$	$28.4^{+6.2}_{-5.2}$	$+0.4^{+0.3}_{-0.3}$	$1.3^{+0.3}_{-0.2}$	$9.3^{+0.2}_{-0.2}$	$3.1^{+0.2}_{-0.2}$	$33.5^{+3.3}_{-2.3}$	$+0.0^{+0.1}_{-0.1}$	11.9
S2COSMOSJ095715+022008	COSMOS	$2.96^{+0.43}_{-0.44}$	$45.2^{+0.2}_{-0.2}$	$1.9^{+2.6}_{-1.3}$	$+0.5^{+1.9}_{-1.0}$	$0.4^{+0.6}_{-0.3}$	$9.3^{+0.1}_{-0.2}$	$3.2^{+0.1}_{-0.2}$	$3.3^{+2.4}_{-3.6}$	$-0.9^{+0.0}_{-0.0}$	10.9
S2CLSJ021915-044408	UDS	$2.38^{+0.24}_{-0.22}$	$44.4^{+0.2}_{-0.2}$	$16.2^{+5.0}_{-3.9}$	$-0.2^{+0.3}_{-0.2}$	$0.8^{+0.2}_{-0.2}$	$9.3^{+0.1}_{-0.1}$	$3.2^{+0.1}_{-0.1}$	—	—	—
S2CLSJ021644-050222	UDS	$2.57^{+0.22}_{-0.21}$	$44.3^{+0.2}_{-0.2}$	$21.8^{+5.6}_{-4.5}$	$+0.1^{+0.3}_{-0.2}$	$1.1^{+0.3}_{-0.2}$	$9.4^{+0.1}_{-0.1}$	$3.2^{+0.1}_{-0.1}$	—	—	—

Table 2. (Continued ...)

IAU	Field	z	P_{UR} %	$\sum \mathcal{F}$	$\delta_{R_{eff}}^{\dagger}$	$\sum \mathcal{P}_{assoc}^{\dagger}$	$\log_{10}(M_{dust})^{\dagger}$ [M_{\odot}]	$\log_{10}(\Psi)^{\dagger}$ [$M_{\odot} \text{ yr}^{-1}$]	$\sum \mathcal{P}_{assoc}$	$\delta_{R_{eff}}$	$\log_{10}(M_{stars})$ [M_{\odot}]
FIR						Optical/NIR					
S2COSMOSJ095835+025327	COSMOS	$2.63^{+0.28}_{-0.26}$	$43.8^{+0.2}_{-0.2}$	$2.9^{+2.8}_{-1.6}$	$-0.6^{+0.4}_{-0.2}$	$0.4^{+0.4}_{-0.2}$	$9.3^{+0.1}_{-0.1}$	$3.1^{+0.1}_{-0.1}$	—	—	—
S2COSMOSJ095947+013659	COSMOS	$2.70^{+0.31}_{-0.28}$	$43.1^{+0.2}_{-0.2}$	$5.9^{+3.5}_{-2.3}$	$-0.1^{+0.5}_{-0.4}$	$0.5^{+0.3}_{-0.2}$	$9.2^{+0.2}_{-0.2}$	$3.1^{+0.1}_{-0.1}$	$22.3^{+2.8}_{-4.2}$	$-0.1^{+0.4}_{-0.2}$	11.5
S2COSMOSJ100013+023429	COSMOS	$2.77^{+0.33}_{-0.29}$	$42.6^{+0.2}_{-0.2}$	$25.6^{+6.1}_{-5.0}$	$+0.4^{+0.3}_{-0.3}$	$1.1^{+0.3}_{-0.2}$	$9.4^{+0.2}_{-0.1}$	$3.2^{+0.2}_{-0.1}$	$28.5^{+3.3}_{-3.7}$	$+0.3^{+0.4}_{-0.3}$	11.6
S2CLSJ021543-050050	UDS	$2.42^{+0.32}_{-0.31}$	$41.9^{+0.2}_{-0.2}$	$11.2^{+4.3}_{-3.2}$	$-0.1^{+0.3}_{-0.3}$	$0.6^{+0.2}_{-0.2}$	$9.2^{+0.2}_{-0.2}$	$3.0^{+0.1}_{-0.2}$	—	—	—
S2CLSJ021931-045826	UDS	$2.83^{+0.36}_{-0.28}$	$41.1^{+0.2}_{-0.2}$	$23.1^{+5.8}_{-4.7}$	$+0.3^{+0.3}_{-0.3}$	$0.7^{+0.2}_{-0.1}$	$9.2^{+0.2}_{-0.2}$	$3.1^{+0.2}_{-0.2}$	$18.6^{+2.1}_{-2.1}$	$+0.0^{+0.1}_{-0.1}$	11.5
S2CLSJ021756-045244	UDS	$2.36^{+0.26}_{-0.24}$	$41.0^{+0.2}_{-0.2}$	$15.2^{+4.8}_{-3.8}$	$-0.2^{+0.2}_{-0.2}$	$0.6^{+0.2}_{-0.2}$	$9.2^{+0.2}_{-0.2}$	$3.0^{+0.1}_{-0.2}$	$29.8^{+3.4}_{-3.2}$	$+0.0^{+0.1}_{-0.1}$	11.7
S2COSMOSJ100202+014453	COSMOS	$3.19^{+0.36}_{-0.31}$	$40.9^{+0.2}_{-0.2}$	$6.7^{+3.6}_{-2.5}$	$+0.0^{+0.5}_{-0.4}$	$0.4^{+0.2}_{-0.1}$	$9.3^{+0.1}_{-0.1}$	$3.2^{+0.1}_{-0.1}$	$10.2^{+2.0}_{-3.3}$	$-0.3^{+0.3}_{-0.2}$	11.2
S2CLSJ021833-052042	UDS	$2.46^{+0.28}_{-0.27}$	$40.7^{+0.2}_{-0.2}$	$26.3^{+6.0}_{-4.9}$	$+0.3^{+0.3}_{-0.3}$	$1.2^{+0.2}_{-0.2}$	$9.3^{+0.2}_{-0.2}$	$3.1^{+0.2}_{-0.2}$	$42.7^{+3.6}_{-2.7}$	$+0.0^{+0.1}_{-0.1}$	11.9
S2COSMOSJ100039+023843	COSMOS	$2.63^{+0.35}_{-0.31}$	$40.5^{+0.2}_{-0.2}$	$15.7^{+5.0}_{-3.9}$	$+0.2^{+0.4}_{-0.2}$	$0.7^{+0.2}_{-0.2}$	$9.2^{+0.2}_{-0.2}$	$3.1^{+0.2}_{-0.2}$	$25.6^{+3.1}_{-4.1}$	$+0.0^{+0.4}_{-0.2}$	11.7
S2COSMOSJ095829+025227	COSMOS	$2.66^{+0.38}_{-0.33}$	$40.3^{+0.2}_{-0.2}$	$5.8^{+3.5}_{-2.3}$	$-0.2^{+0.5}_{-0.3}$	$0.5^{+0.3}_{-0.2}$	$9.1^{+0.2}_{-0.2}$	$3.0^{+0.1}_{-0.2}$	—	—	—
S2COSMOSJ100340+023638	COSMOS	$2.65^{+0.34}_{-0.37}$	$39.6^{+0.2}_{-0.2}$	$2.0^{+2.6}_{-1.3}$	$+0.9^{+2.5}_{-1.2}$	$0.9^{+1.1}_{-0.9}$	$9.4^{+0.1}_{-0.2}$	$3.2^{+0.1}_{-0.2}$	—	—	—
S2COSMOSJ100242+021407	COSMOS	$2.61^{+0.30}_{-0.26}$	$39.5^{+0.2}_{-0.2}$	$7.8^{+3.9}_{-2.7}$	$-0.2^{+0.4}_{-0.3}$	$0.5^{+0.3}_{-0.2}$	$9.2^{+0.1}_{-0.2}$	$3.1^{+0.1}_{-0.2}$	$37.3^{+3.3}_{-4.4}$	$+0.0^{+0.5}_{-0.2}$	11.8
S2CLSJ021803-045526	UDS	$2.87^{+0.27}_{-0.24}$	$39.0^{+0.2}_{-0.2}$	$20.7^{+5.4}_{-4.4}$	$+0.0^{+0.3}_{-0.2}$	$0.6^{+0.2}_{-0.1}$	$9.5^{+0.1}_{-0.1}$	$3.2^{+0.1}_{-0.1}$	$18.8^{+1.7}_{-2.7}$	$-0.0^{+0.1}_{-0.1}$	11.4
S2CLSJ021921-052716	UDS	$2.52^{+0.25}_{-0.23}$	$38.8^{+0.2}_{-0.2}$	$11.5^{+4.4}_{-3.3}$	$+0.2^{+0.5}_{-0.3}$	$0.6^{+0.2}_{-0.2}$	$9.2^{+0.1}_{-0.1}$	$3.1^{+0.1}_{-0.2}$	—	—	—
S2COSMOSJ100252+024159	COSMOS	$2.57^{+0.23}_{-0.18}$	$38.7^{+0.2}_{-0.2}$	$4.9^{+3.3}_{-2.1}$	$-0.3^{+0.5}_{-0.3}$	$0.6^{+0.2}_{-0.3}$	$9.5^{+0.1}_{-0.1}$	$3.4^{+0.1}_{-0.1}$	$40.7^{+3.7}_{-4.4}$	$-0.0^{+0.4}_{-0.2}$	11.8
S2COSMOSJ100117+014247	COSMOS	$2.90^{+0.26}_{-0.25}$	$38.1^{+0.2}_{-0.2}$	$8.7^{+4.0}_{-2.9}$	$+0.2^{+0.5}_{-0.4}$	$0.5^{+0.2}_{-0.2}$	$9.4^{+0.1}_{-0.1}$	$3.2^{+0.1}_{-0.1}$	$38.8^{+3.7}_{-2.9}$	$+0.1^{+0.4}_{-0.2}$	11.7
S2CLSJ141557+520711	EGS	$3.21^{+0.41}_{-0.31}$	$37.9^{+0.2}_{-0.2}$	$4.7^{+3.2}_{-2.0}$	$-0.4^{+0.4}_{-0.2}$	$0.1^{+0.1}_{-0.1}$	$9.3^{+0.1}_{-0.1}$	$3.2^{+0.1}_{-0.1}$	—	—	—
S2COSMOSJ100252+022903	COSMOS	$2.59^{+0.29}_{-0.27}$	$37.7^{+0.2}_{-0.2}$	$6.7^{+3.6}_{-2.5}$	$-0.1^{+0.5}_{-0.3}$	$0.6^{+0.3}_{-0.2}$	$9.3^{+0.1}_{-0.1}$	$3.1^{+0.1}_{-0.1}$	$33.7^{+2.9}_{-4.1}$	$-0.2^{+0.3}_{-0.2}$	11.8
S2CLSJ021600-045938	UDS	$2.34^{+0.28}_{-0.25}$	$37.3^{+0.2}_{-0.2}$	$19.8^{+5.3}_{-4.3}$	$+0.1^{+0.3}_{-0.2}$	$1.1^{+0.3}_{-0.2}$	$9.3^{+0.2}_{-0.2}$	$3.1^{+0.2}_{-0.2}$	—	—	—
S2CLSJ021931-052156	UDS	$2.44^{+0.32}_{-0.28}$	$36.6^{+0.2}_{-0.2}$	$11.3^{+4.3}_{-3.2}$	$+0.4^{+0.5}_{-0.4}$	$0.5^{+0.2}_{-0.1}$	$9.1^{+0.2}_{-0.2}$	$3.0^{+0.2}_{-0.2}$	—	—	—
S2COSMOSJ095921+014737	COSMOS	$2.78^{+0.30}_{-0.27}$	$36.5^{+0.2}_{-0.2}$	$4.7^{+3.2}_{-2.0}$	$-0.3^{+0.5}_{-0.3}$	$0.4^{+0.3}_{-0.2}$	$9.2^{+0.1}_{-0.1}$	$3.1^{+0.1}_{-0.1}$	$35.0^{+2.3}_{-4.4}$	$+0.0^{+0.4}_{-0.2}$	11.8
S2COSMOSJ095759+014111	COSMOS	$3.00^{+0.46}_{-0.36}$	$36.4^{+0.2}_{-0.2}$	$1.9^{+2.5}_{-1.2}$	$-0.7^{+0.4}_{-0.2}$	$0.3^{+0.4}_{-0.2}$	$9.1^{+0.2}_{-0.2}$	$3.0^{+0.2}_{-0.2}$	$32.5^{+1.8}_{-3.8}$	$+0.1^{+0.4}_{-0.2}$	11.7
S2COSMOSJ095942+022937	COSMOS	$3.27^{+0.34}_{-0.29}$	$36.4^{+0.2}_{-0.2}$	$12.5^{+4.5}_{-3.4}$	$-0.1^{+0.3}_{-0.3}$	$0.4^{+0.1}_{-0.1}$	$9.4^{+0.1}_{-0.1}$	$3.3^{+0.1}_{-0.1}$	$20.3^{+1.8}_{-3.0}$	$+0.3^{+0.5}_{-0.3}$	11.4
S2CLSJ141826+524154	EGS	$2.96^{+0.41}_{-0.31}$	$36.0^{+0.2}_{-0.2}$	$20.2^{+5.4}_{-4.4}$	$+0.2^{+0.3}_{-0.3}$	$0.6^{+0.2}_{-0.1}$	$9.2^{+0.2}_{-0.2}$	$3.1^{+0.2}_{-0.2}$	—	—	—
S2COSMOSJ100141+022713	COSMOS	$3.39^{+0.36}_{-0.37}$	$36.0^{+0.2}_{-0.2}$	$7.8^{+3.9}_{-2.7}$	$-0.1^{+0.5}_{-0.3}$	$0.3^{+0.1}_{-0.1}$	$9.6^{+0.1}_{-0.1}$	$3.4^{+0.1}_{-0.1}$	$27.4^{+1.7}_{-2.5}$	$+0.2^{+0.4}_{-0.2}$	11.7
S2COSMOSJ095958+023459	COSMOS	$2.98^{+0.37}_{-0.29}$	$35.9^{+0.2}_{-0.2}$	$20.5^{+5.5}_{-4.4}$	$+0.5^{+0.4}_{-0.3}$	$0.7^{+0.2}_{-0.1}$	$9.2^{+0.2}_{-0.2}$	$3.1^{+0.2}_{-0.2}$	$22.7^{+2.7}_{-3.1}$	$+0.2^{+0.5}_{-0.3}$	11.6
S2COSMOSJ095922+025137	COSMOS	$3.41^{+0.43}_{-0.35}$	$35.9^{+0.2}_{-0.2}$	$6.8^{+3.7}_{-2.5}$	$+0.1^{+0.6}_{-0.4}$	$0.3^{+0.2}_{-0.1}$	$9.6^{+0.1}_{-0.1}$	$3.3^{+0.1}_{-0.1}$	—	—	—
S2CLSJ021805-051050	UDS	$3.63^{+0.41}_{-0.32}$	$35.5^{+0.2}_{-0.2}$	$24.2^{+5.7}_{-4.7}$	$+0.2^{+0.3}_{-0.2}$	$0.4^{+0.1}_{-0.1}$	$9.5^{+0.1}_{-0.1}$	$3.3^{+0.2}_{-0.1}$	$7.3^{+0.8}_{-0.6}$	$+0.0^{+0.1}_{-0.1}$	11.1
S2COSMOSJ095936+020419	COSMOS	$2.44^{+0.26}_{-0.25}$	$35.4^{+0.2}_{-0.2}$	$7.8^{+3.8}_{-2.7}$	$-0.2^{+0.4}_{-0.3}$	$0.5^{+0.3}_{-0.2}$	$9.2^{+0.2}_{-0.2}$	$3.0^{+0.1}_{-0.2}$	$37.2^{+2.5}_{-5.8}$	$+0.1^{+0.4}_{-0.2}$	11.8
S2CLSJ021822-050738	UDS	$2.98^{+0.43}_{-0.32}$	$35.2^{+0.2}_{-0.2}$	$16.4^{+4.9}_{-3.8}$	$-0.1^{+0.3}_{-0.2}$	$0.5^{+0.2}_{-0.1}$	$9.2^{+0.2}_{-0.2}$	$3.0^{+0.2}_{-0.2}$	$25.5^{+1.2}_{-2.3}$	$-0.0^{+0.1}_{-0.1}$	11.6

[†] These parameters have been adjusted to account for ‘missing’ DSFGs.

Note. — Ultra-Red galaxies are listed in decreasing order of ultra-red probability.

As discussed, ultra-red galaxies appear to preferentially signpost over-densities of DSFGs and furthermore they appear to be situated near to the centres of medium-to-high-value over-density peaks. Thus, this motivated us to examine the optical/NIR environments around these ultra-red galaxies, with the aim to uncover any relationships that may, or may not, be present within such extreme environments at $z \gtrsim 3$. For instance, has the emergence of the red sequence taken place around ultra-red galaxies at these redshifts yet? Or, is there any dependence on the colour and/or stellar mass of galaxies as the radial distance from an ultra-red galaxy varies? If these relationships are not uncovered, it may suggest that something is wrong with our understanding of the formation of massive galaxies at high redshift and the role that they play in the assembly of large structure.

4.1 Optical/NIR Data Acquisition

To answer these questions, we made use of publicly available, multi-wavelength catalogues covering the COSMOS⁶ (McCracken et al. 2012; Laigle et al. 2016) and UDS⁷ fields (Almaini et al., in prep.). Although such catalogues do exist for the EGS and GOODS-N fields, their coverage does not include the regions occupied by the ultra-red galaxies presented within this chapter. As for the remaining fields, to the best of our knowledge, there are no available optical/NIR data.

The catalogue for the COSMOS field contains 606,887 sources within an area of $\mathcal{A} \approx 1.70 \text{ deg}^2$ that comprises the UltraVISTA-DR2 region. The catalogue for the UDS field contains 184,439 sources detected over an area of $\mathcal{A} \approx 0.77 \text{ deg}^2$ that comprises the 8th release (Hartley et al. 2013) of the United Kingdom IR Telescope (UKIRT) IR Deep Sky Survey (UKIDSS — Lawrence et al. 2007). Therefore, the surveyed area for both of these fields is slightly smaller than that surveyed by SCUBA-2. Hence, although there are 59 ultra-red galaxies within the COSMOS and UDS fields, there is only suitable optical/NIR coverage for 42 ultra-red galaxies; 30 from the COSMOS field and 12 from the UDS field.

For both of the fields, the photometric redshifts contained within the catalogues were computed using a χ^2 -minimisation code (Arnouts et al. 1999) over a redshift grid of $0 < z_{\text{phot}} < 6$ down to a resolution of $\delta z_{\text{phot}} = 0.01$. The implementation of this code used a combination of template SEDs (representing spiral, elliptical and young, blue star-forming galaxies), appropriately handled galactic dust extinction and was found to produce an intrinsic scatter of $\sigma_{\Delta z} = 0.021(1+z)$ at $z > 3$ – far better than that achieved with the FIR template SEDs adopted here. However, over $z \sim 0\text{--}3$ the median upper and lower fitting uncertainties for these galaxies increases by a factor of $\sim 5 \times$ to $\sigma_{z_{\text{NIR}}}^+ = 0.11$ and $\sigma_{z_{\text{NIR}}}^- = 0.23$, respectively, which dwarfs this intrinsic scatter. We modelled each photometric redshift in the catalogue using a split-normal distribution defined as:

$$P = A \exp \begin{cases} -(z_{\text{phot}} - z_{\text{NIR}})^2 / 2(\sigma_{z_{\text{NIR}}}^+)^2 & \text{if } z_{\text{phot}} > z_{\text{NIR}} \\ -(z_{\text{phot}} - z_{\text{NIR}})^2 / 2(\sigma_{z_{\text{NIR}}}^-)^2 & \text{otherwise,} \end{cases} \quad (11)$$

where $A = \sqrt{2/\pi} / (\sigma_{z_{\text{NIR}}}^+ + \sigma_{z_{\text{NIR}}}^-)$ integral normalises this distribution and z_{phot} is the redshift grid covering $0 < z_{\text{phot}} < 10$ down to a resolution of $\delta z_{\text{phot}} = 0.01$, i.e. mimicking that used for DSFGs in Paper I, Paper II and here.

These catalogues also provide absolute magnitudes (M) and stellar masses (M_{stars}). The former were either taken directly from the best-fitting, rest-frame template SED, or K -corrected from the apparent magnitude (m) measured through the passband closest to $\lambda_M(1+z)$. Stellar masses were typically derived by scaling (in the observed frame) large samples of synthetic spectra to the K -band apparent magnitude and taking the resulting modal (or best-fit) stellar mass of these spectra (e.g. Mortlock et al. 2013, 2015).

LBGs around ultra-red galaxies at $z \sim 3$ should have limited-to-no data at wavelengths shorter than the central wavelength of U/B bands due to the Lyman- α break at $1,216 \text{ \AA}$ causing them to ‘drop-out’ of these passbands. Thus, in order to ensure that the LBGs used in this analysis had robust stellar mass and/or absolute magnitude estimates, we required that their detected K -band photometry was below the $(3\text{--}5)\text{-}\sigma_K$ limiting magnitude. To further increase the completeness of this sample, we also required that their photometric redshifts were ‘satisfactory’ (i.e. consistent with having a galaxy-shaped SED and a suitable χ^2 value) and that their stellar masses were above $M_{\text{stars}} > 10^9 M_{\odot}$.

In Table 3, we list the FITS binary field names and respective values necessary to implement these constraints on the catalogues, which reduce the number of sources in the COSMOS and UDS fields to 201,376 and 61,750, respectively.

4.2 Robust Counterparts to DSFGs

In order to determine which LBGs were associated to the environments around the ultra-red galaxies presented here, we needed to first examine whether there were any underlying systematics between the FIR photometric redshifts (z_{FIR}) and those provided in the catalogues discussed above (z_{NIR}). To test for such systematics, we first matched all of the available DSFGs to their true (or ‘real’) counterparts.

In this work, we adopted the likelihood ratio (LR — Chapin et al. 2011; Fleuren et al. 2012; McAlpine et al. 2013) method in order to locate potential counterparts to DSFGs, which is defined as:

$$\text{LR} = \frac{\text{Probability of being related}}{\text{Probability of being unrelated}} = \frac{f(r, \mathcal{R})q(K, z)}{n(K, z)}, \quad (12)$$

where $q(K, z)$ and $n(K, z)$ are the K -band magnitude and redshift prior distributions of the real counterparts to DSFGs and background galaxies, respectively, and

$$f(r, \mathcal{R}) = \frac{1}{2\pi\mathcal{R}^2} \exp(-r^2/\mathcal{R}^2)$$

is a Gaussian weighting that takes into account the positional accuracy of a given DSFG. The positional accuracy is capped above $\mathcal{R} \geq 2''$ (i.e. the SCUBA-2 pixel scale) to avoid $\mathcal{R} \rightarrow 0$ for those DSFGs detected at a high SNR. Furthermore, as it is typically much greater than that deduced for optical/NIR galaxies (i.e. $\mathcal{R} < 0.2''$), we do not add it (in quadrature) to the radial offset for DSFGs.

⁶ http://ftp.iap.fr/pub/from_users/hjmcc/COSMOS2015/COSMOS2015_optical_NIR_galaxies

⁷ http://www.nottingham.ac.uk/~ppzoa/cls/UDS_DR8_forS2CLS_v4_data.html

Table 3. COSMOS and UDS catalogue flags.

FITS field name	Value	FITS field name	Value	Description
..... COSMOS.....	 UDS.....		
TYPE	0	Basic galaxy catalogue	T	Galaxy SED shape
ZPDF	> 0	chisq_at_maxL	≤ 15	Satisfactory z_{phot}
Ksw_MAG_APER2	< 24.5	MAG_APER_K_2.0	< 24.6	K-Band cut
MASS_BEST	> 9	Bestfit_Mass	> 9	Stellar-Mass cut
FLAG_HJMCC	0	—		UltraVISTA-DR2

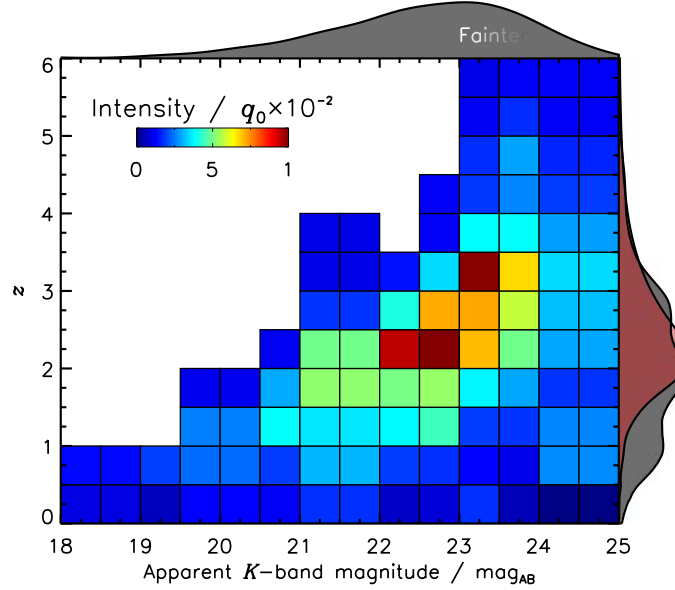


Figure 7. The two-dimensional prior distribution for potential optical/NIR counterparts to 829 DSFGs in the COSMOS field as a function of apparent K -band magnitude and redshift. This prior distribution was used to determine the LR that a given galaxy is the real counterpart to a given DSFG (see equation (12)). We show the K -band magnitude distribution towards the top of the plot, which clearly shows that counterparts to DSFGs are faint, with K -band magnitudes peaking at $K \sim 23 \text{ mag}_{\text{AB}}$ (or $S_K \sim 2 \times 10^{-3} \text{ mJy}$). To the right, we show the photometric redshift distributions for the potential NIR counterparts (dark grey) and DSFGs (red, see 2). The two distributions appear to be well matched around $z \sim 2-3$, but seriously mismatched at $z \sim 1$, which results in an extended tail of K -band magnitudes below $K \lesssim 20 \text{ mag}_{\text{AB}}$. This mismatch is likely caused by the incorrect assignation of foreground galaxies to distant DSFGs. **Note.** Fainter apparent K -band magnitudes correspond to brighter galaxies.

We estimated the prior distributions of the counterparts and background galaxies as follows.

- Firstly, we search for all galaxies within an $r_{\text{aper}} = 8$ -arcsec radius of a given DSFG. Such a conservatively sized search radius accounts for the fact that some of the brightest DSFGs originally catalogued in the S2CLS UDS field were found to be offset by up to half of a SCUBA-2 PSF FWHM from their high-resolution counterparts detected with ALMA (i.e. by as much as $\theta/2 \approx 8''$ — Simpson et al. 2015).

- For any detected galaxies around a given DSFG, we select those that have apparent K -band magnitudes between K' and $K' + \Delta K'$ (with K' ranging from $K' = 18-25 \text{ mag}_{\text{AB}}$ and $\Delta K' = 0.5 \text{ mag}_{\text{AB}}$) and sum their respective photometric redshift distributions represented by equation (11). Performing this process for all DSFGs generates a two-dimensional ‘total(K, z)’ image, which contains a contribution from the ‘background’ galaxies and from the ‘real’ counterparts, i.e.

$$\text{total}(K, z) = \text{background}(K, z) + \text{real}(K, z).$$

- To determine the contribution from the background galaxies, the above steps are repeated but this time replacing the positions of the DSFGs with 10,000 randomly generated positions. Normalising this background contribution by the area of the search radius, yields the prior distribution for the background galaxies, i.e.

$$n(K, z) = \frac{\text{background}(K, z)}{\pi r_{\text{aper}}^2}.$$

- Finally, the prior distribution for the real counterparts to the DSFGs can be determined by:

$$q(K, z) = q_0 \left(\frac{\text{real}(K, z)}{\sum_i \text{real}(K_i, z_i)} \right),$$

where $q_0 = 69 \pm 4\%$ is a normalisation factor that estimates the probability of finding a real counterpart down to the $5\text{-}\sigma \lesssim 24 \text{ mag}_{\text{AB}}$ survey limit, i.e. $\sim 70\%$ of DSFGs have a real counterpart in the catalogues used here⁸.

⁸ q_0 was indirectly determined from a model fit of the form

In Fig. 7, we show $q(K, z)$ for the potential counterparts to 829 DSFGs in the COSMOS field, noting that a similar prior distribution is derived for the UDS field. Clearly the counterparts to DSFGs are faint, with typical K -band magnitudes of $K \sim 23 \text{ mag}_{\text{AB}}$ (or equivalently $S_K \sim 2 \times 10^{-3} \text{ mJy}$, i.e. a factor of $\gtrsim 3,000\times$ fainter than at $850 \mu\text{m}$ for these DSFGs) – similar to that seen in Simpson et al. (2014). Although the optical/NIR and FIR photometric redshift distribution appear to be well matched around $z \sim 2\text{--}3$, there is a serious mismatch towards $z \sim 1$, which results in an extended tail below $K \lesssim 20 \text{ mag}_{\text{AB}}$. This is likely caused by foreground (brighter) galaxies that have been incorrectly assigned as a real counterpart to a DSFG. These incorrect assignments occur because either the real counterpart is too faint to be detected or (in extremely rare cases) outside of the 8-arcsec search radius. As these incorrect matches will heavily skew any future analysis, they needed to be removed before comparing the FIR with the optical/NIR photometric redshift estimates.

To decide which counterparts to remove, we compared the LR for the DSFGs already computed to those of a large control sample. This large control sample was generated by calculating the LR for each DSFG after the centre of its search radius had been randomly tweaked. The top-panel of Fig. 8 shows the distribution of LR for DSFGs and this large control sample. We highlight the LR that gives a false-positive rate of 10%, which was determined by integrating the tail of the control sample. This false-positive rate corresponds to a LR of LR = 1.3, above which only $\sim 50\%$ of DSFGs have a real counterpart.

We then evaluated the normalised difference,

$$\Delta z / (1 + z_{\text{FIR}}) \equiv (z_{\text{NIR}} - z_{\text{FIR}}) / (1 + z_{\text{FIR}}),$$

for each of these DSFG with a counterpart, which is shown in the bottom-panel of Fig. 8. We obtained a LR-weighted mean and LR-weighted standard deviation of $\mu_{\Delta z} = +0.04(1 + z_{\text{FIR}})$ and $\sigma_{\Delta z} = 0.17(1 + z_{\text{FIR}})$, respectively, for these real counterparts. This suggests that the FIR photometric redshifts presented here slightly under-estimate the optical/NIR photometric redshifts by $\mu_{\Delta z} = 0.16$ at $z = 3$, although this correction is intrinsically uncertain to $\sigma_{\Delta z} = 0.68$. Thus, before we evaluated the association probabilities of LBGs around ultra-red galaxies using equation (10), we shifted the FIR photometric redshift distribution of the ultra-red galaxies by $+0.04(1 + z_{\text{FIR}})$, where z_{FIR} was taken from the peak of a given FIR photometric redshift distribution.

4.3 Stellar Masses and Absolute Colours of LBGs

With knowledge of how the FIR photometric redshifts correlate with the optical/NIR photometric redshifts, we examined the stellar masses (M_{stars}) and absolute ($M_B - M_I$) colours of the LBGs surrounding the ultra-red galaxies presented in this work. To recap, there are 42 ultra-red galaxies

($1 - q_0 f(r_{\text{aper}})$) to the ratio of blank apertures (i.e. apertures containing no galaxies) around DSFGs to those around random positions as a function of aperture radius from $r_{\text{aper}} = 0\text{--}10''$. However, as we later normalise the LR by a factor dependent on the false-positive rate of ‘real’ counterparts, determining q_0 in this way is not strictly necessary.

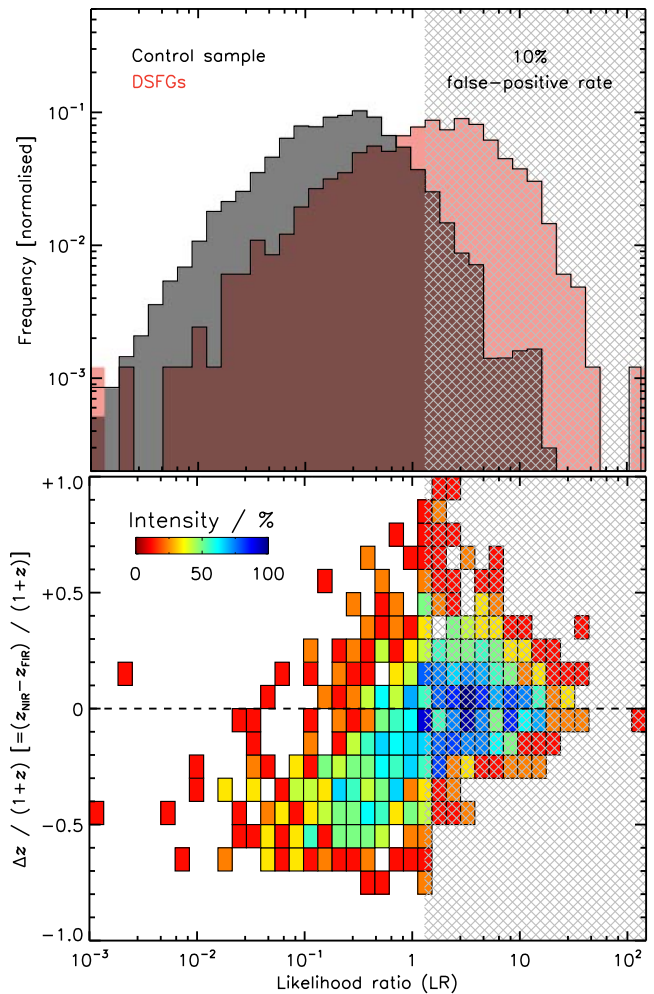


Figure 8. Top: histogram of the LR for potential optical/NIR counterparts to DSFGs catalogued in the COSMOS field (black), which we compared to random positions (red). This comparison results in a false-positive rate of 10% above a LR of $\gtrsim 1.3$ (chequered light grey region). Only 50% of DSFGs in the COSMOS field have a potential counter above this LR. **Bottom:** normalised difference, $(z_{\text{NIR}} - z_{\text{FIR}}) / (1 + z_{\text{FIR}})$, as a function of LR, between photometric redshifts determined using optical/NIR and FIR photometry. We obtain a LR-weighted mean and LR-weighted standard deviation of $\mu_{\Delta z} = +0.04(1 + z_{\text{FIR}})$ and $\sigma_{\Delta z} = 0.17(1 + z_{\text{FIR}})$, respectively, for potential counterparts above $\text{LR} \gtrsim 1.3$. Therefore, the FIR photometric redshifts presented here slightly under-estimate the optical/NIR photometric redshifts by $\mu_{\Delta z} = 0.16$ at $z = 3$, although this correction is uncertain to $\sigma_{\Delta z} = 0.68$. Potential counterparts with LR less than $\text{LR} < 1$, have FIR photometric redshifts that are significantly higher than the optical/NIR ones – suggesting that they are likely foreground galaxies.

with optical/NIR coverage, 30 within the COSMOS field and 12 within the UDS field.

At the positions of each of these ultra-red galaxies, we extracted all of LBGs that lie within a radius of $R_{\text{eff}} \approx 5'$ and recorded their stellar masses, absolute M_B and M_I magnitudes, probability of being associated (to the ‘adjusted’ FIR photometric redshift) using equation (10) and radial distances to these positions. We also generated a control sample for each ultra-red galaxy by extracting the same properties

but at 100 random positions, purposefully selected to avoid any overlap with the ultra-red galaxies.

On average, there are ≈ 28 LBGs that are ‘associated’ to given ultra-red galaxy, but this varies considerably from ≈ 3 –53. Although this only accounts for $\sim 1\%$ of the optical/NIR galaxies that are typically within $R_{\text{eff}} \approx 5'$ of an ultra-red galaxy, this is still a factor of $\sim 20\times$ the number of DSFGs that we were able to associate. Thus, the contribution from surrounding LBGs is definitely not insignificant and, like for the associated DSFGs, is probably underestimated here, too.

4.3.1 Stellar Masses

In Fig. 9, we show the stellar masses of the surrounding LBGs weighted by their association probability as a function of proper radial distance to their respective central ultra-red galaxies (assuming that they reside at $z \sim 3$). The average stellar mass in annuli of equal area shows a slight decrease from $(4.7 \pm 0.4) \times 10^{10} M_{\odot}$ at ≈ 60 kpc to $(1.1 \pm 0.1) \times 10^{10} M_{\odot}$ at ≈ 400 kpc. Furthermore, the average $(M_B - M_I)$ -colour decreases from 0.57 ± 0.02 at ≈ 60 kpc to 0.28 ± 0.02 at ≈ 400 kpc, too. Although modest in size, these trends suggest that the ultra-red galaxies are residing near the centres of potential wells extending over $\lesssim 500$ kpc scales, and that these environmental factors are causing a factor of $\sim 4\times$ and $\sim 2\times$ increase in the stellar masses and colours of the surrounding LBGs, respectively. At larger distances from the ultra-red galaxies, the average stellar masses of the LBGs fluctuates around the control average of $M_{\text{stars}} = (1.62 \pm 0.05) \times 10^{10} M_{\odot}$, which itself shows no significant change in each annuli (as might be expected for a control sample).

Although some of the contribution to the central annulus will be influenced by the presence of the ultra-red galaxies themselves, which on occasions will have multiple possible counterparts (due to the multiplicity of DSFGs), it is very unlikely that the ≈ 140 kpc (or $\sim 20''$) annulus will contain the real LBG counterparts to any of these ultra-red galaxies. The average stellar mass and colour in this annulus are $(3.8 \pm 0.4) \times 10^{10} M_{\odot}$ and 0.52 ± 0.03 , respectively, which is still a factor of $\sim 3.5\times$ and $\sim 2\times$ increase in the stellar masses and colours of the surrounding LBGs, respectively.

Finally, the average total stellar mass from $K \lesssim 24$ -mag_{AB} LBGs within the vicinity of ultra-red galaxies is $\sum M_{\text{stars}} = 4.7 \times 10^{11} M_{\odot}$, though this ranges by two orders of magnitude from 7.8×10^{10} – $1.1 \times 10^{12} M_{\odot}$ (in-line with the range of the associated number of LBGs). Thus, the potential total $z \sim 0$ stellar mass of these candidate proto-clusters is $\sim 8 \times 10^{11} M_{\odot}$ – assuming that the DSFGs convert all of their molecular gas into stars and their 850- μm flux densities have not been severely boosted by chance gravitational lensing. Although very much a lower limit, these total stellar masses correspond to DM halos with masses of $M_{\text{halo}} \sim 10^{14}$ – $10^{15} M_{\odot}$ (Behroozi et al. 2013) – similar to those observed for Fornax-/Virgo-type galaxy clusters.

4.3.2 Absolute Colours

The absolute M_B and M_I magnitudes allow a quantitative measure on whether the red sequence has emerged around

ultra-red galaxies as they are suitably positioned at either ends of the optical spectrum, which additionally allows any future comparisons with local galaxy clusters to be made. Furthermore, at $z \sim 3$ these colours are derived from the $\approx J$ -/ K -band apparent magnitudes, which we have placed sufficient constraints on to ensure that these measurements are both reliable and complete. Thus, for each ultra-red galaxy, we evaluated the CDF for the $(M_B - M_I)$ colours of the surrounding LBGs, again weighted by their association probability. In the bottom-panel of Fig. 10, we show the average of these CDFs for all of 42 ultra-red galaxies and their respective control samples. A K-S test using equation (8) yielded a value of $D_{\text{K-S}} = 0.21$ – equating to a probability of $P_{\text{K-S}} \sim 2\%$ that the control and ultra-red galaxy samples are drawn from the same distribution.

As an aid, in the top-panel of Fig. 10, we show the approximate locations of the red/blue sequences and the so-called ‘green valley’ at $z < 1$ and $2 < z < 5$, each modelled as a Gaussian distribution. The peak of the blue sequence and green valley galaxies appears to have been shifted towards bluer colours at earlier epochs – suggestive of a younger stellar population.

This aid highlights that there is a $\gtrsim 1\text{-}\sigma$ deficit in blue-sequence galaxies around ultra-red galaxies. Furthermore, this deficit is continued far into the colour space occupied by the green-valley galaxies, which suggests that the emergence of the red sequence is happening at a faster rate around ultra-red galaxies than in the (control) field.

4.3.3 Could the Surrounding NIR/Optical Galaxies Just be Dusty?

Although tentative evidence of the accelerated emergence of a red sequence around ultra-red galaxies has been presented in the previous section, we now analyse whether this same result could be achieved if the surrounding NIR/optical galaxies were simply dustier in composition, rather than ‘dead’ in nature.

As the process of star formation increases the dust content in the ISM of star-bursting galaxies experiencing enhanced star formation, it is very plausible that the excess of red galaxies seen residing around ultra-red galaxies is due to a dustier population. Such a scenario could hint at the presence of some large-scale mechanism capable of simultaneously enhancing the star formation across multiple galaxies within a dense environment (see Paper II).

The variation of extinction with passband is usually defined using the R_V parameter that takes into account the ratio of V - and B -band extinction, or A_V and A_B , respectively, as follows:

$$R_V \equiv \frac{A_V}{A_B} - 1, \quad (13)$$

For the Milky Way or a starburst-like galaxy, R_V typically ranges from 3.1–3.2. The magnitudes of extinction experienced by the B - and I -bands assuming a value of $R_V = 3.1$ are listed in Table 4. Hence, the $(M_B - M_I)$ -colour extinction (or $A_B - A_I$) can be defined as a function of V -band extinction as follows:

$$A_B - A_I = (1.321 - 0.594)A_V \approx 0.7A_V, \quad (14)$$

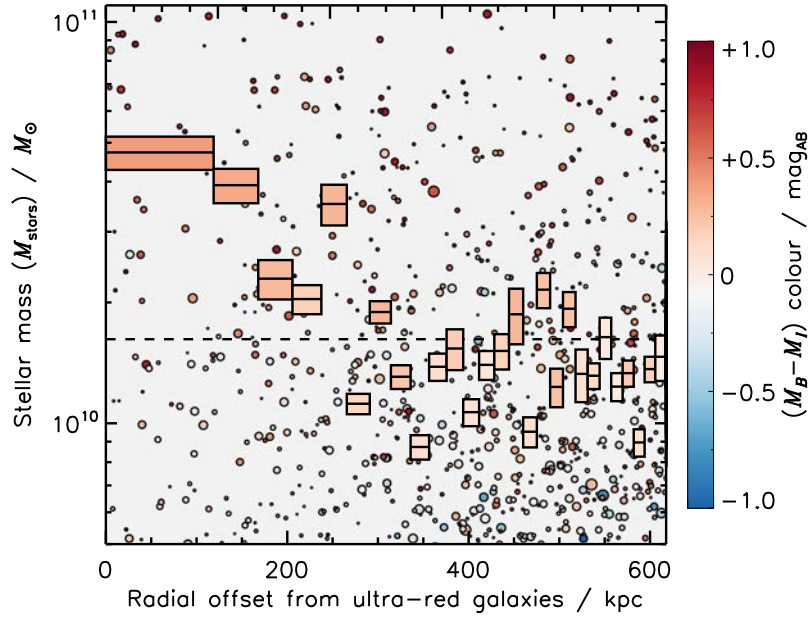


Figure 9. Stellar mass and absolute colour variations of LBGs within $\lesssim 500$ kpc of their respective central ultra-red galaxies. Individual stellar mass measurements of the surrounding LBGs are represented as circles, colour-coded to represent their absolute $(M_B - M_I)$ colour and scaled to represent their association probability to their respective ultra-red galaxies. We show the average and standard error of the stellar mass within annuli of equal area. This figure illustrates that as the radial distance from an ultra-red galaxy increases out to ~ 400 kpc, the average stellar mass decreases by a factor of $\sim 4\times$ to $M_{\text{stars}} = (1.1 \pm 0.1) \times 10^{10} M_{\odot}$. This increasing average stellar mass with radius suggests that ultra-red galaxies reside in over-dense environments. The black dashed line shows the typical annuli average stellar mass from the control sample $M_{\text{stars}} = (1.62 \pm 0.05) \times 10^{10} M_{\odot}$. **Note.** This figure assumes that all ultra-red galaxies are lying at $z \sim 3$, where $1'$ corresponds to ≈ 470 kpc.

Table 4. Magnitudes of extinction for the B - and I -band photometry assuming the $R_V = 3.1$ extinction laws of Cardelli et al. (1989) and O'Donnell (1994). **Note.** These data were obtained from Table 6 in Schlegel et al. (1998).

Facility	Filter	$1/\lambda_{\text{eff}}$ μm^{-1}	$A_{\lambda_{\text{eff}}}/A_V$
Subaru Suprime-Cam	B	2.3	1.3
Subaru Suprime-Cam	I	1.2	0.6

or equivalently, the $(M_B - M_I)$ colour is reddened by $\approx 70\%$ of the V -band obscuration experienced by a given galaxy.

In Fig. 11, we show the effect of increasing the A_V extinction on the $(M_B - M_I)$ colour for the control sample by $A_V = (0-1) \text{ mag}_{\text{AB}}$. Clearly evident is that $A_V = 1 \text{ mag}_{\text{AB}}$ of extinction shifts the control sample to a redder $(M_B - M_I)$ colour (by $\approx 0.5 \text{ mag}_{\text{AB}}$) than compared to the ultra-red galaxies.

Performing a least-squares fit to the A_V -corrected, $(M_B - M_I)$ colour of the control sample against the $(M_B - M_I)$ colour of the ultra-red galaxies yields a value of $A_V \sim (0.26 \pm 0.05) \text{ mag}_{\text{AB}}$. Thus, the control sample *could* be mapped onto the ultra-red galaxy sample if it was to experience a very moderate dust reddening of $A_V \sim 0.3 \text{ mag}_{\text{AB}}$.

Thus, it is very plausible that the optical/NIR galaxies surrounding ultra-red galaxies are experiencing enhanced star formation that is slightly increasing the amount of dust within their ISM.

4.4 Over-Densities of LBGs

We computed the optical/NIR over-density parameters around the ultra-red galaxies by comparing the number of massive $M_{\text{stars}} > 10^{10} M_{\odot}$ galaxies residing in their 5-arcmin environments to that expected from the field. Throughout this calculation, we took into account the varying instrumental noise and edge effects by ‘conserving’ the number of pixels within each 5-arcmin aperture around the positions of ultra-red galaxies and their respective control samples.

In Fig. 12, we show how these optical/NIR over-densities vary as a function of the FIR over-densities computed previously. Thus, it would appear that not all over-densities of DSFGs equate to over-densities of LBGs, at least not *strongly* since there does appear to be a *slight* tilt in the contours, which may suggest that they may correlate weakly. However, only $\sim 60\%$ of the 32 ultra-red galaxies with available optical/NIR data reside in over-dense regions of the Universe, and of these, only $\sim 60\%$ are over-dense in LBGs. Or put another way, only a third of ultra-red galaxies appear to be over-dense in both DSFGs and LBGs. Overall though, $\sim 80\%$ of ultra-red galaxies signpost regions that are either over-dense in DSFGs, or LBGs or both.

5 CONCLUSION

In this paper, we have presented a multi-wavelength analysis of 64 ultra-red galaxies – selected via their ultra-red probabilities – within the S2CLS and S2COSMOS imaging surveys.

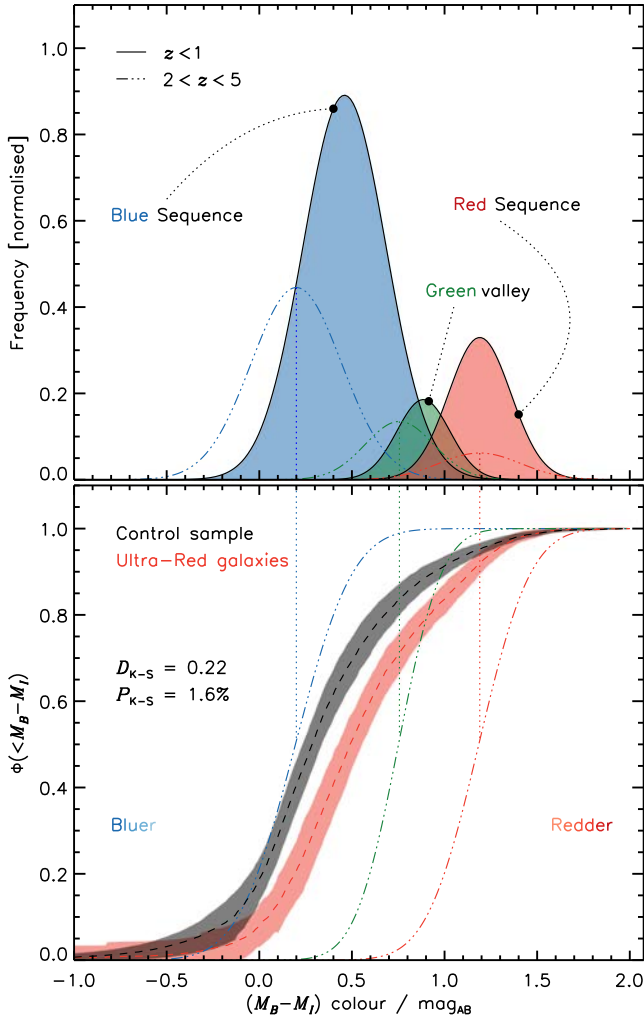


Figure 10. Top: empirically derived Gaussian distributions representing the red/blue sequences and so-called ‘green valley’ at $z < 1$ (solid lines) and $z \approx 2-5$ (dashed lines). The distributions for the blue sequence and green valley are shifted to relatively bluer colours at $z \approx 2-5$ compared to $z < 1$ – reflecting the prevalence of a younger stellar at these distant epochs. The peaks of these distributions at $z \approx 2-5$ are indicated by dotted lines as an aid to the bottom panel of this figure. **Bottom:** CDF of the $(M_B - M_I)$ colour for LBGs detected within $R_{\text{eff}} \approx 5'$ of an ultra-red galaxy (red) or a random control position (black). LBGs from both samples have been weighted by their respective association probabilities using equation (10). The CDFs for ultra-red galaxies and the control sample diverge around $(M_B - M_I) = 0.0-1.0$, which suggests that there is a larger number of red-sequence LBGs in the vicinity of ultra-red galaxies than compared

We found that just over half of these ultra-red galaxies reside in over-dense regions of DSFGs. In terms of global FIR over-density peaks, it appears that ultra-red galaxies play a central ($< a$ few megaparsec) role in medium-value global over-density peaks. By weighting each DSFG by its probability of being associated to the central ultra-red galaxy, we found that the average total dust masses surrounding these ultra-red galaxies was $\sim 2 \times 10^9 M_\odot$ (having been corrected for the ‘missing’ DSFGs within their vicinities). These values are consistent with those reported in Paper II. However, we were still only able to associate ≈ 1 surrounding DSFG to its

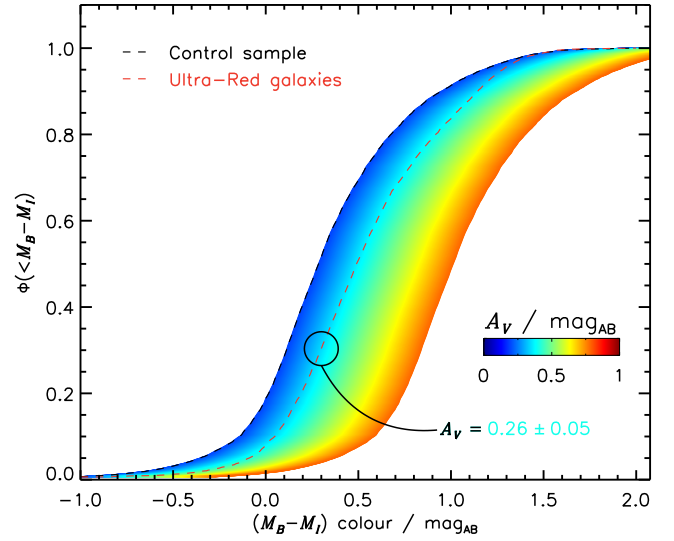


Figure 11. CDFs of the $(M_B - M_I)$ colour for the control sample and the ultra-red galaxies as shown in Fig. 10. We adjust the $(M_B - M_I)$ colours of the control sample to account for varying amounts of V-band extinction up to $A_V = 1 \text{ mag}_{\text{AB}}$ shown by the shaded region. Indicated by a black circle is the best-fit value of the extinction corrected CDF of the $(M_B - M_I)$ colour for the control sample to that of the ultra-red galaxies. This best-fit, least-squares value suggests that the control sample could be mapped onto the ultra-red galaxy sample if they were to experience a very moderate dust reddening of $A_V \sim 0.3 \text{ mag}_{\text{AB}}$.

central ultra-red galaxy using this new association method, which perhaps suggests that this is the limit achievable with FIR-based photometric redshifts.

Using optical/NIR ground-based data (down to $5\text{-}\sigma_K$ depths of $\lesssim 24 \text{ mag}_{\text{AB}}$) for 32 ultra-red galaxies within the COSMOS and UDS fields, we were able to associate an average of ≈ 28 LBGs to within $\lesssim 5'$ of a given ultra-red galaxy – a factor of $\sim 30\times$ the number of DSFGs. These associated LBGs showed a factor of $\approx 5\times$ increase in stellar mass and a factor of $3\times$ increase in absolute $(M_B - M_I)$ colour as their distance to the ultra-red galaxies decreased over $\approx 500 \text{ kpc}$ (or $\approx 2'$) scales. This suggests that the red sequence has already emerged, or is beginning to emerge, around these ultra-red galaxies at $z \sim 3$. In particular, there appears to be a higher fraction of green-valley galaxies around ultra-red galaxies than compared to the field, supporting the concept that, on average, the red sequence is emerging at a faster rate around ultra-red galaxies. With an average total stellar mass contribution from the LBGs of $4.7 \times 10^{11} M_\odot$, and assuming that the ultra-red galaxies convert all of their molecular gas into stars, these candidate, high-redshift proto-clusters have the potential to form systems with stellar masses of at least $M_{\text{stars}} \sim 10^{12} M_\odot$ by $z \sim 0$.

Thus, we have shown that there is a sizeable contribution from LBGs to these high-redshift systems signposted by ultra-red galaxies. Although these systems have average optical/NIR/FIR properties that are consistent with their evolution into present-day galaxy clusters with DM halos of mass $M_{\text{halo}} \sim 10^{14}-10^{15} M_\odot$, we are still likely missing a sizeable contribution from LBGs that my association probability has failed to associate. Therefore, the results presented here should be regarded as firm lower limits on the opti-

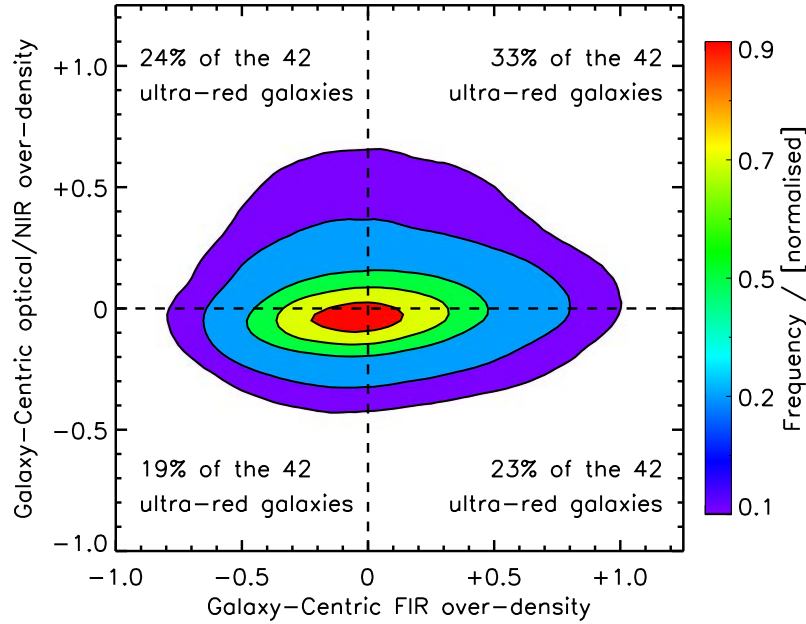


Figure 12. Optical/NIR versus FIR over-densities for the 42 ultra-red galaxies with optical/NIR data. **Note.** The comparatively low over-density parameter values reported here are due to the large apertures over which they are measured that effectively dilutes the signal from all but the largest over-densities.

cal/NIR/FIR properties of the environments around ultra-red galaxies, which can now only be improved upon when spectroscopic data increases the accuracy of the redshift estimates.

ACKNOWLEDGEMENTS

AJRL and RJI acknowledge support from the European Research Council (ERC) in the form of Advanced Grant, 321302, COSMICISM. This research has made use of data from *HerMES* project (<http://hermes.sussex.ac.uk/>). *HerMES* is a *Herschel* Key Programme utilizing Guaranteed Time from the SPIRE instrument team, ESAC scientists and a mission scientist. The JCMT is operated by the East Asian Observatory on behalf of The National Astronomical Observatory of Japan, Academia Sinica Institute of Astronomy and Astrophysics, the Korea Astronomy and Space Science Institute, the National Astronomical Observatories of China and the Chinese Academy of Sciences (Grant No. XDB090000000), with additional funding support from STFC and participating universities in the UK and Canada; Program ID MJLSC0.

REFERENCES

- Arnouts S., Cristiani S., Moscardini L., Matarrese S., Lucchin F., Fontana A., Giallongo E., 1999, *MNRAS*, **310**, 540
- Aversa R., Lapi A., de Zotti G., Shankar F., Danese L., 2015, *ApJ*, **810**, 74
- Baldry I. K., Glazebrook K., Brinkmann J., Ivezić Ž., Lupton R. H., Nichol R. C., Szalay A. S., 2004, *ApJ*, **600**, 681
- Barger A. J., Cowie L. L., Sanders D. B., Fulton E., Taniguchi Y., Sato Y., Kawara K., Okuda H., 1998, *Nature*, **394**, 248
- Barlow R., 2004, ArXiv Physics e-prints,
- Baugh C. M., Lacey C. G., Frenk C. S., Granato G. L., Silva L., Bressan A., Benson A. J., Cole S., 2005, *MNRAS*, **356**, 1191
- Behroozi P. S., Wechsler R. H., Conroy C., 2013, *ApJ*, **770**, 57
- Blain A. W., Chapman S. C., Smail I., Ivison R., 2004, *ApJ*, **611**, 725
- Bower R. G., Kodama T., Terlevich A., 1998, *MNRAS*, **299**, 1193
- Capak P. L., et al., 2011, *Nature*, **470**, 233
- Cardelli J. A., Clayton G. C., Mathis J. S., 1989, *ApJ*, **345**, 245
- Casali M., et al., 2007, *A&A*, **467**, 777
- Casey C. M., 2016, *ApJ*, **824**, 36
- Casey C. M., et al., 2015, *ApJ*, **808**, L33
- Chabrier G., 2003, *ApJ*, **586**, L133
- Chapin E. L., et al., 2011, *MNRAS*, **411**, 505
- Chapman S. C., Blain A., Ibatana R., Ivison R. J., Smail I., Morrison G., 2009, *ApJ*, **691**, 560
- Chiang Y.-K., Overzier R., Gebhardt K., 2013, *ApJ*, **779**, 127
- Cox P., et al., 2011, *ApJ*, **740**, 63
- Dempsey J. T., et al., 2013, *MNRAS*, **430**, 2534
- Dey A., Lee K.-S., Reddy N., Cooper M., Inami H., Hong S., Gonzalez A. H., Jannuzi B. T., 2016, *ApJ*, **823**, 11
- Dickey J. M., Lockman F. J., 1990, *ARA&A*, **28**, 215
- Dressler A., et al., 1997, *ApJ*, **490**, 577
- Eales S., Lilly S., Gear W., Dunne L., Bond J. R., Hammer F., Le Fèvre O., Crampton D., 1999, *ApJ*, **515**, 518
- Eales S., et al., 2010, *PASP*, **122**, 499
- Fleuren S., et al., 2012, *MNRAS*, **423**, 2407
- Geach J. E., et al., 2017, *MNRAS*, **465**, 1789
- Gerke B. F., et al., 2007, *MNRAS*, **376**, 1425
- Gialalisco M., 2002, *ARA&A*, **40**, 579
- Griffin M. J., et al., 2010, *A&A*, **518**, L3
- Groth E. J., Kristian J. A., Lynds R., O’Neil Jr. E. J., Balsano R., Rhodes J., WFPC-1 IDT 1994, in American Astronomical Society Meeting Abstracts. p. 1403
- Hartley W. G., et al., 2013, *MNRAS*, **431**, 3045
- Hayward C. C., Narayanan D., Kereš D., Jonsson P., Hopkins P. F., Cox T. J., Hernquist L., 2013, *MNRAS*, **428**, 2529
- Hinshaw G., et al., 2009, *ApJS*, **180**, 225
- Holland W. S., et al., 1999, *MNRAS*, **303**, 659
- Holland W. S., et al., 2013, *MNRAS*, **430**, 2513

Hughes D. H., et al., 1998, *Nature*, **394**, 241
 Hung C.-L., et al., 2016, *ApJ*, **826**, 130
 Ibar E., et al., 2010, *MNRAS*, **409**, 38
 Ikarashi S., et al., 2011, *MNRAS*, **415**, 3081
 Ivison R. J., et al., 2007, *MNRAS*, **380**, 199
 Ivison R. J., et al., 2016, *ApJ*, **832**, 78
 Kennicutt Jr. R. C., 1998, *ARA&A*, **36**, 189
 Kreysa E., et al., 1998, in Phillips T. G., ed., Proc. SPIE Vol. 3357, Advanced Technology MMW, Radio, and Terahertz Telescopes. pp 319–325
 Laigle C., et al., 2016, *ApJS*, **224**, 24
 Lapi A., Raimundo S., Aversa R., Cai Z.-Y., Negrello M., Celotti A., De Zotti G., Danese L., 2014, *ApJ*, **782**, 69
 Lawrence A., et al., 2007, *MNRAS*, **379**, 1599
 Lewis A. J. R., et al., 2018, *ApJ*, **862**, 96
 Lilly S. J., Cowie L. L., Gardner J. P., 1991, *ApJ*, **369**, 79
 Lutz D., et al., 2011, *A&A*, **532**, A90
 Markwardt C. B., 2009, in Bohlender D. A., Durand D., Dowler P., eds, Astronomical Society of the Pacific Conference Series Vol. 411, Astronomical Data Analysis Software and Systems XVIII. p. 251 ([arXiv:0902.2850](#))
 McAlpine K., Jarvis M. J., Bonfield D. G., 2013, *MNRAS*, **436**, 1084
 McCracken H. J., et al., 2012, *A&A*, **544**, A156
 Michałowski M. J., et al., 2017, *MNRAS*, **469**, 492
 Mortlock A., et al., 2013, *MNRAS*, **433**, 1185
 Mortlock A., et al., 2015, *MNRAS*, **447**, 2
 Negrello M., et al., 2010, *Science*, **330**, 800
 Nguyen H. T., et al., 2010, *A&A*, **518**, L5
 O'Donnell J. E., 1994, *ApJ*, **422**, 158
 Overzier R. A., Guo Q., Kauffmann G., De Lucia G., Bouwens R., Lemson G., 2009, *MNRAS*, **394**, 577
 Peebles P. J. E., Yu J. T., 1970, *ApJ*, **162**, 815
 Pilbratt G. L., et al., 2010, *A&A*, **518**, L1+
 Pope A., et al., 2008, *ApJ*, **675**, 1171
 Riechers D. A., et al., 2010, *ApJ*, **720**, L131
 Robertson B., Li Y., Cox T. J., Hernquist L., Hopkins P. F., 2007, *ApJ*, **667**, 60
 Romano D., Matteucci F., Zhang Z.-Y., Papadopoulos P. P., Ivison R. J., 2017, *MNRAS*, **470**, 401
 Safarzadeh M., Lu Y., Hayward C. C., 2017, preprint, ([arXiv:1705.05377](#))
 Schlegel D. J., Finkbeiner D. P., Davis M., 1998, *ApJ*, **500**, 525
 Scoville N., et al., 2007, *ApJS*, **172**, 1
 Simpson J. M., et al., 2014, *ApJ*, **788**, 125
 Simpson J. M., et al., 2015, *ApJ*, **799**, 81
 Smail I., Ivison R. J., Blain A. W., 1997, *ApJ*, **490**, L5+
 Spergel D. N., et al., 2003, *ApJS*, **148**, 175
 Springel V., et al., 2005, *Nature*, **435**, 629
 Steidel C. C., Giavalisco M., Pettini M., Dickinson M., Adelberger K. L., 1996, *ApJ*, **462**, L17
 Straatman C. M. S., et al., 2014, *ApJ*, **783**, L14
 Takagi T., et al., 2009, in Onaka T., White G. J., Nakagawa T., Yamamura I., eds, Astronomical Society of the Pacific Conference Series Vol. 418, AKARI, a Light to Illuminate the Misty Universe. p. 275
 Venemans B. P., et al., 2007, *A&A*, **461**, 823
 Wang W.-H., Cowie L. L., Barger A. J., 2004, *ApJ*, **613**, 655
 Zhang Z.-Y., Romano D., Ivison R. J., Papadopoulos P. P., Matteucci F., 2018, preprint, ([arXiv:1806.01280](#))

APPENDIX A: ULTRA-RED OVER-DENSITY AND HERSCHEL SPIRE CUT-OUTS

In this Appendix, we present the over-density and *Herschel* SPIRE cut-outs for the remaining ultra-red galaxies with $P_{\text{UR}} > 60\%$.

This paper has been typeset from a \LaTeX file prepared by the author.

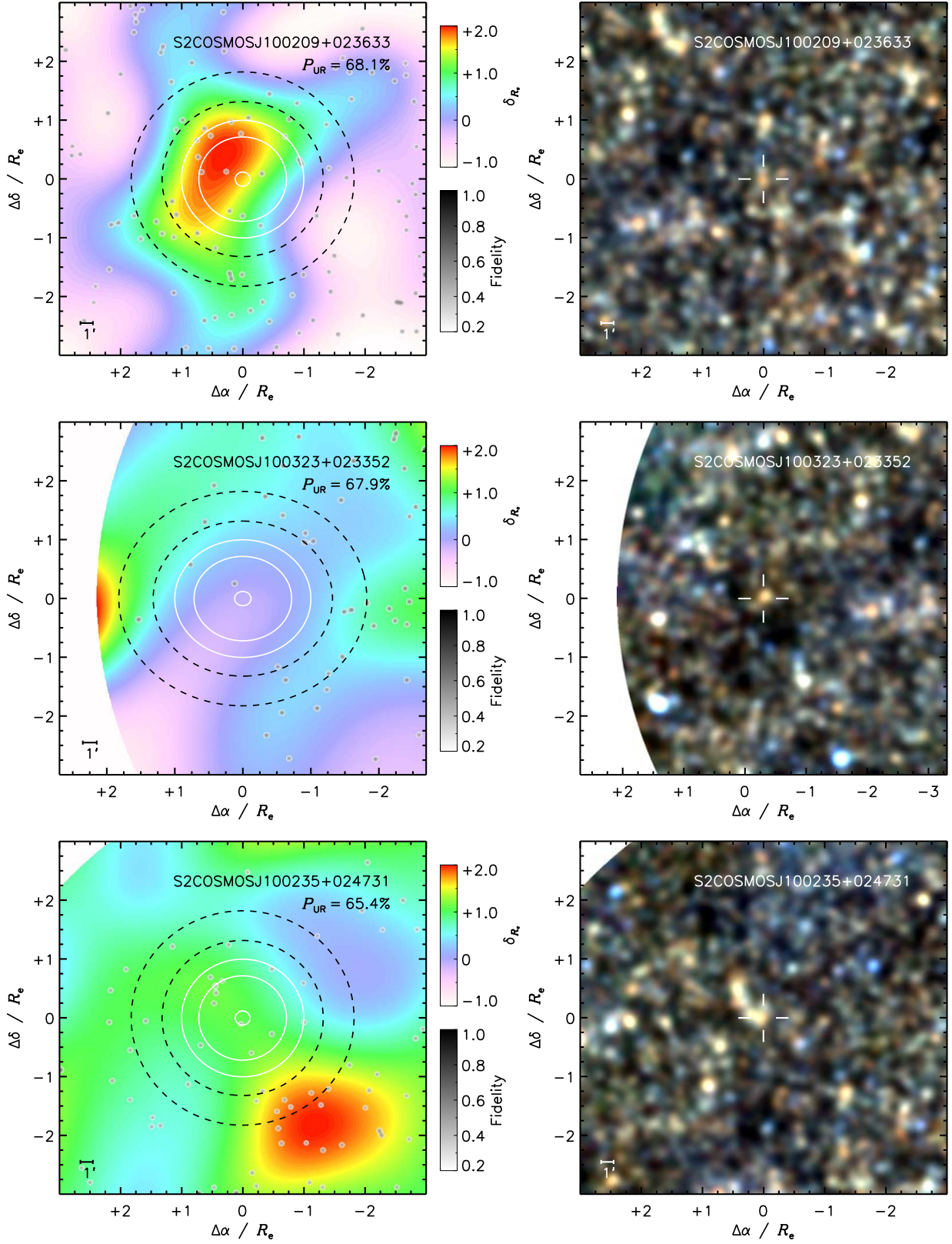


Figure A1. Continuation of Fig. 4 ...

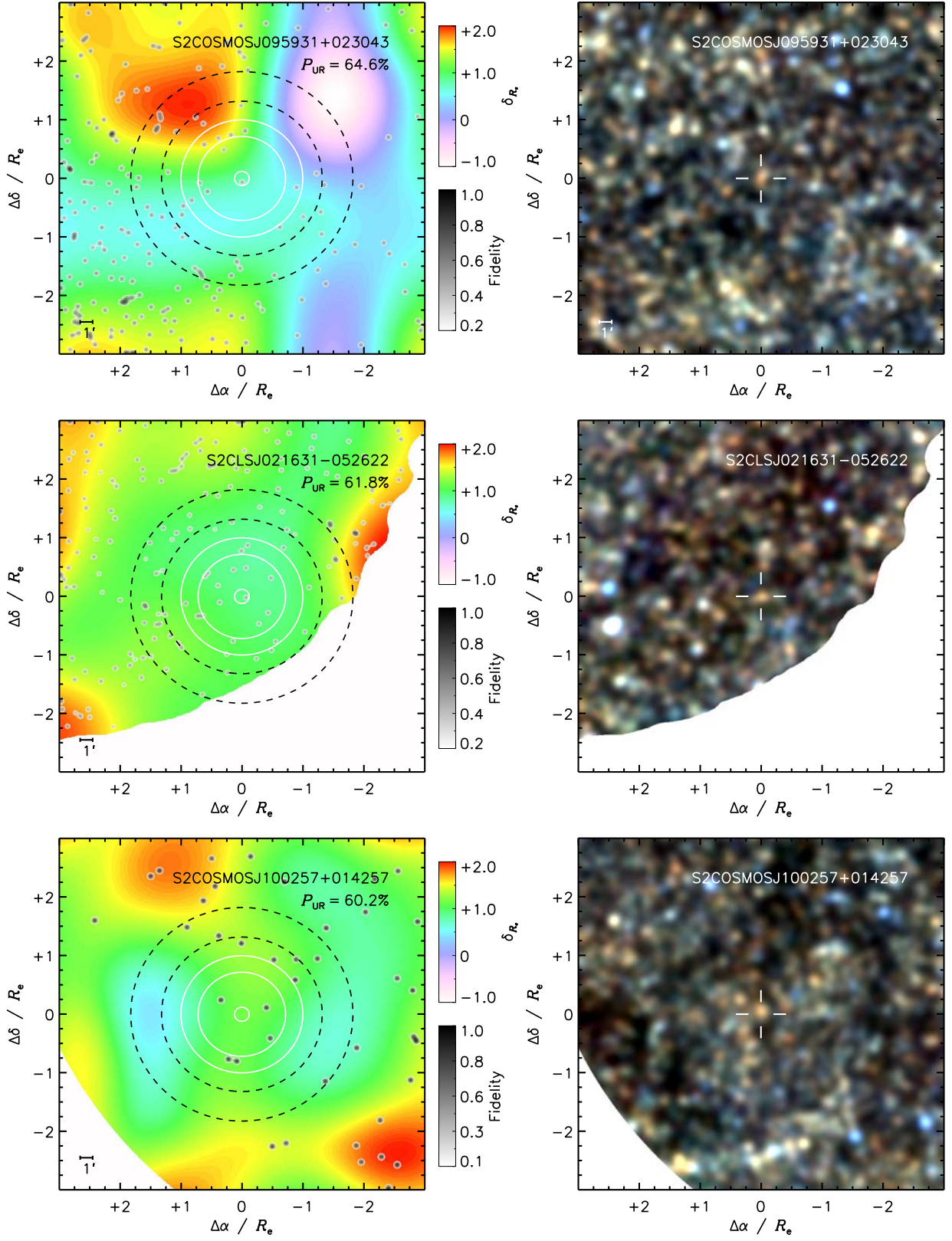


Figure A1. Continuation of Fig. 4 ...